Metavalent Bonding in Crystalline Solids: How Does It Collapse?

Ludovica Guarneri, Stefan Jakobs, A von Hoegen, Stefan Maier, Ming Xu, Min Zhu, Sophia Wahl, Christian Teichrib, Yiming Zhou, Oana Cojocaru-mirédin, et al.

Metavalent bonding in crystalline solids: how does it collapse?

L. Guarneri[1,*], S. Jakobs[1,*], A. von Hoegen[1,*], S. Maier[1], M. Xu[1], M. Zhu[1], S. Wahl[1], C. Teichrib[1], Y. Zhou[1], O. Cojocaru-Mirédin[1], M. Raghuwanshi[1], C.-F. Schön[1], M. Drögeler[2], C. Stampfer[2,3], R. P. S. M. Lobo[4a,4b], A. Piarristeguy[5], A. Pradel[5], J.-Y. Raty[6], M. Wuttig[1,3,7]

[1] RWTH Aachen University, I. Physikalisches Institut (IA), 52056 Aachen, Germany

[2] RWTH Aachen University, II. Physikalisches Institut (IIA), 52056 Aachen, Germany

[3] JARA-FIT and JARA-HPC, RWTH Aachen University, 52056 Aachen, Germany

[4a] LPEM, ESPCI Paris, CNRS, PSL University; 10 rue Vauquelin, F-75005 Paris, France

[4b] Sorbonne Université, ESPCI Paris, CNRS, LPEM, F-75005 Paris, France

[5] ICGM, Univ. Montpellier, CNRS, ENSCM, F-34095 Montpellier, France

[6] CESAM and Physics of Solids, Interfaces and Nanostructures, B5, Université de Liège, B4000 Sart-Tilman, Belgium

[7] PGI 10 (Green IT), Forschungszentrum Jülich, 52428 Jülich, Germany

The chemical bond is one of the most powerful, yet much debated concepts in chemistry, explaining property trends in solids. Recently, a novel type of chemical bonding has been identified in several higher chalcogenides, characterized by a unique property portfolio, unconventional bond breaking and sharing of about one electron between adjacent atoms. This metavalent bond is a fundamental type of bonding in solids besides covalent, ionic and metallic bonding, raising the pertinent question, if there is a well-defined transition between metavalent and covalent bonds. Here we study three different pseudo-binary lines, namely $GeTe_{1-x}Se_x$, $Sb_2Te_{3(1-x)}Se_{3x}$ and $Bi_{2-2x}Sb_{2x}Se_3$, and evidence a sudden change in several properties, including optical absorption $\varepsilon_2(\omega)$, optical dielectric constant ε_∞, Born effective charge Z*, electrical conductivity as well as bond breaking behavior for a critical Se or Sb concentration. These findings provide a blueprint to experimentally explore the influence of metavalent bonding on attractive properties of phase change materials and thermoelectrics. Particularly important is its impact on optical properties, which can be tailored by the amount of electrons shared between adjacent atoms. This correlation can be employed to design opto-electronic materials and to explore systematic changes in chemical bonding with stoichiometry and atomic arrangement.

Keywords: metavalent bonding, phase change materials, thermoelectrics, topological insulators, atom probe tomography, bond breaking, materials by design, property map

* These authors contributed equally.

The development of the periodic table of the elements by Mendeleev and Meyer more than 150 years ago revealed characteristic property trends if the elements are sorted accordingly.[1] [2] Moving down a column in the periodic table frequently leads to a transition from a non-metal to a metal. This can be nicely seen in the carbon group 14 of the periodic table, where the move from C, Si (covalently bonded) to Ge, Sn and Pb leads to a transition to a metallic ground state (Pb). Interestingly, a similar transition is also observed for the group 15 elements, i.e. the pnictogens, where P is covalently bonded, but Sb and Bi are (semi)-metals. This raises questions concerning the nature of the transition from covalent (CB) to metallic bonding (MB). With this work we contribute to answering these questions by discussing the transition from the recently defined "metavalent bond" [3] to the covalent bond. The former is located between the metallic and the covalent bond, but has a portfolio of properties that differs significantly from both, which makes it rather unconventional. The groundwork for defining and understanding metavalent bonding (MVB) has already been laid.[3] It has been demonstrated that metavalently bonded solids are characterized by a unique combination of properties, including a pronounced anharmonicity (i.e. a large mode-specific Grüneisen parameter (γ_i) of the optical phonons), moderate electrical conductivities (σ), effective coordination numbers (ECoN) incompatible with the traditional '8-N' view of covalent bonding, a large chemical bond polarizability, leading to high values of the Born effective charge (Z*) as well as a large optical dielectric constant (ε_∞).[4] Indeed, the idea of metavalent solids characterized by a unique set of properties has recently found further support from a quantum-chemical bond analysis in conjunction with machine learning. Based on this approach, it was possible to discriminate between covalent, metavalent and metallically bonded solids[5]. Metavalent materials are also characterized by an unusual bond rupture observed by atom probe tomography.[6] So far, experimental findings and arguments in favor of MVB have been reported for several sesqui-chalcogenides including Bi_2Te_3, Bi_2Se_3 and Sb_2Te_3, while Sb_2Se_3, Sb_2Se_3 and Bi_2S_3 were shown not to utilize MVB[7]. Similarly, mono-chalcogenides based on Ge, Sn and Pb have been studied [8] [9]. All three tellurides were identified as metavalent solids, while among the selenides and sulfides only PbSe and PbS showed MVB [9]. Furthermore, $AgSbTe_2$ reveals MVB as can be seen from the

position in the map, its bond rupture and the high Born effective charge and the large value of ε_∞ [10]. Upon applying pressure or temperature, several solids apparently show a transition to a denser, metavalently bonded phase, as shown explicitly for As_2Se_3[11]. It seems reasonable to assume that all mono-chalcogenides (i.e. SnSe, SnS, GeSe and GeS) as well as all sesqui-chalcogenides, which did not show MVB at ambient conditions (Bi_2S_3, Sb_2Se_3, Sb_2S_3, As_2S_3) should show MVB at sufficiently large pressures. At the same time, it has also been demonstrated that for some compounds which possess MVB at ambient conditions, high pressures can destroy it [12]. In general, MVB should be possible, whenever two atoms are held together by a σ–bond created by a single p-electron. Such a situation is encountered also for halide perovskites, where the Sn-I and Pb-I bond, respectively also shows the characteristic features of metavalent bonds [13]

Quantum chemical calculations confirm the presence and stability of an unconventional type of bonding in solids, where about one electron is shared between adjacent atoms, leading to a bond order of about ½, which is in striking contrast to ordinary covalent bonding, where the bond order is about 1 and two electrons are shared between adjacent atoms [10]. All of these findings suggest a distinct nature of metavalent bonding. Nevertheless, it is critical, to verify or refute this hypothesis through carefully designed experiments. Such experiments are not only needed to further substantiate the claims of a novel, fundamental type of bonding. They are also important to understand the relationship between applications of chalcogenides and similar solids in phase change memories, thermoelectrics and photovoltaics and the prevailing bonding mechanism. Very recently, for example, it has been argued[14] that rhombohedral GeSe, which shows favorable thermoelectric properties utilizes metavalent bonding, while the orthorhombic phase of GeSe does not. Such findings call for a systematic exploration of the transition between metavalent and covalent bonding. If metavalent bonding is a fundamental bonding mechanism in solids, distinctively different from covalent bonding, then one expects to find representative properties, where the transition between metavalent and covalent bonding is characterized by an abrupt property change. If metavalent bonding is instead a variant of covalent bonding, we expect to find a rather continuous change for all relevant properties.

These different scenarios are depicted and discussed in the supplement (**Fig. S1**). To answer this question, we explore the nature of the MVB-CB transition in three different material systems: $GeTe_{1-x}Se_x$, $Sb_2Te_{3(1-x)}Se_{3x}$ and $Bi_{2-2x}Sb_{2x}Se_3$.

Fig. 1 shows a quantum mechanical map, which is capable of distinguishing metallic, covalent and ionic materials as shown previously.[10] The map is spanned by two coordinates which are determined from calculations based on the quantum theory of atoms in molecules (QTAIM)[15]: the electron transfer (ET) and the number of electrons shared (ES) between pairs of adjacent atoms.[10] The electron transfer is determined by integrating the net charge density of an atom over its basin and subtracting the charge of the free reference atom.[16] The relative electron transfer is obtained upon dividing the total electron transfer by the most common oxidation state. The electron-sharing is derived from the so-called (de-)localization indices.[17]

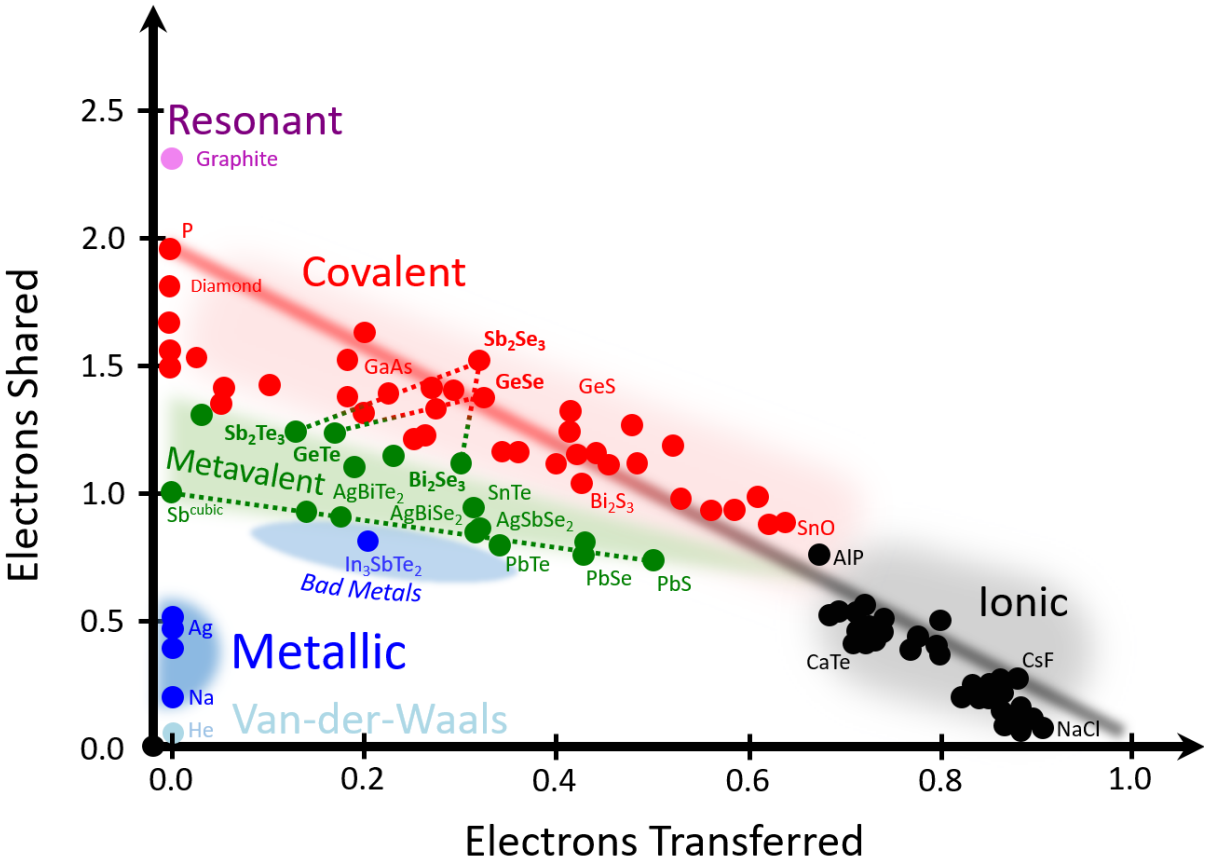

Fig. 1: 2D map classifying chemical bonding in solids. The map is spanned by the number of electrons shared between adjacent atoms and the electron transfer renormalized by the formal oxidation state. The dotted lines denote the three material systems studied here, i.e. the pseudo-binary lines from GeTe to GeSe, from Sb_2Te_3 to Sb_2Se_3 and from Bi_2Se_3 to Sb_2Se_3. All three enable studying the nature of the transition from metavalent (green) to covalent (red) bonding. The nature of the transition can be

captured by studying the (dis-)continuity of the transition in the multidimensional property space. Metallic compounds can be located right below the dashed green line. Map revised after [10].

These two coordinates allow to separate different types of chemical bonding in solids. Ionic materials are characterized by a significant relative electron transfer, typically larger than 0.5; but a rather modest sharing of electrons between adjacent atoms. Consequently, these materials are located in the lower right corner of the map. In covalent compounds, on the contrary, there is vanishing or only modest transfer of electrons between atoms, but up to 2 electrons (i.e. the classical electron pair defined by Lewis)[18] [19] are shared between neighbouring atoms. Metals finally are characterized by a small charge transfer but also only share a modest number of electrons between adjacent atoms, since the electrons are delocalized over several neighbours.

A number of physical properties have been identified as being characteristic for certain types of chemical bonds.[4] For MVB materials, these properties include a large optical dielectric constant ε_∞, together with high Born effective charges (Z*).[20] The former is a measure for the electronic polarizability of the valence electrons, while the latter describes the chemical bond polarizability. The dielectric properties are thus characterized by a pronounced polarizability above and below the highest phonon frequency. Recently, it has also been demonstrated, that pronounced changes in the imaginary part of the dielectric function $\varepsilon_2(\omega)$ can be used to follow changes in chemical bonding.[21] Hence, it is interesting to follow changes in ε_∞ as well as Z* together with $\varepsilon_2(\omega)$ along the pseudo-binary lines from GeTe to GeSe, Sb_2Te_3 to Sb_2Se_3 as well as Bi_2Se_3 to Sb_2Se_3 since these can be correlated with changes in chemical bonding. By studying solid solutions, we are able to tune the stoichiometry in minute steps. This is mandatory to explore the nature of the transition between covalent and metavalent bonding.

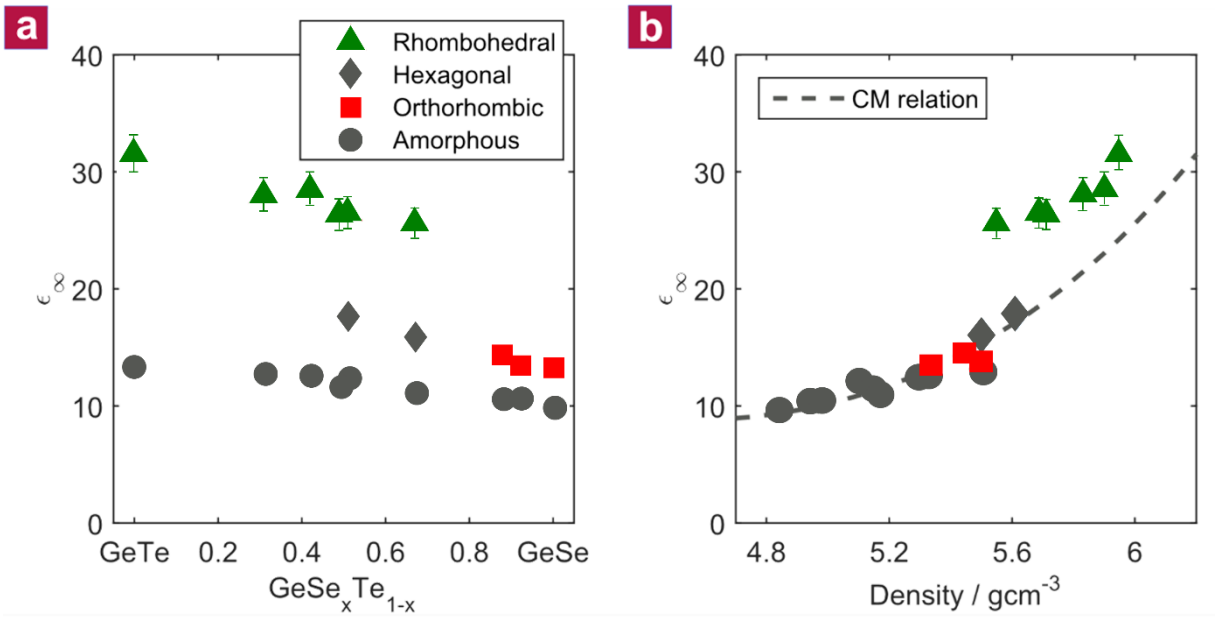

Fig. 2: Optical dielectric constant ε∞ along the pseudo-binary line between GeTe and GeSe: a), ε∞ as a function of stoichiometry. The rhombohedral phase, found up to 70% Se, is characterized by large values of ε∞, which exceed the value of the corresponding amorphous phases by more than 100%. Between 50% and 70% Se-content the rhombohedral phase is metastable and transforms into a hexagonal phase upon further heating. This transition is accompanied by a pronounced drop in ε∞. **b), ε∞** plotted as a function of density. The data for the amorphous, orthorhombic and hexagonal phase follow the Clausius-Mossotti (CM) relation (dashed line), which relates ε∞ and the mass density of the material. Only the rhombohedral phase shows an excess of the electronic polarizability and hence ε∞, characteristic for metavalent bonding.

To determine ε∞, one of the properties to characterize bonding, a sequence of Fourier transform infrared (FTIR) spectra have been recorded for $GeTe_{1-x}Se_x$ thin films. As shown in **Fig. S2** of the supplement, x-ray diffraction (XRD) measurements of compounds along the pseudo-binary line between GeTe and GeSe reveal three different crystallographic phases (rhombohedral, hexagonal and orthorhombic). The linear decrease of the cell volume as a function of stoichiometry is displayed in **Fig. S3** of the supplement, which is strong evidence for the good miscibility of GeTe and GeSe, consistent with previous studies of bulk alloys.[22] [23] From the measured reflectance and transmittance spectra, the dielectric function is determined. The resulting optical dielectric constant ε∞, which is the value of the dielectric function above the highest phonon frequency, is shown in **Fig. 2**.

Two findings are striking in this figure. A pronounced difference between the amorphous and crystalline phase is only observed for the Te-rich, rhombohedral phase. Furthermore, upon the transition from the rhombohedral to the hexagonal and the orthorhombic crystalline phase, a sudden drop in ε_∞ is found. To derive electronic polarizabilities, which are indicative for the bonding mechanism, the density of the solid has to be taken into account, as expressed by the Clausius-Mossotti relation.[24] X-ray reflectometry (XRR) was used to rule out a discontinuous change of the mass density due to the different atomic arrangement in the rhombohedral and hexagonal/orthorhombic phases. The density smoothly decreases with increasing concentration of GeSe (see **Fig. S4** in the supplement). A plot of ε_∞ versus the mass density is displayed in **Fig. 2b**. The dashed line represents a least-squares fit considering only the covalently bonded systems (amorphous, hexagonal and orthorhombic phases) using one set of atomic electronic polarizabilities (*cf.* supplement). All these compounds follow the Clausius-Mossotti relation.[24] On the contrary, all compounds with a rhombohedral crystal structure show an excess in ε_∞, which cannot be explained by their higher density. Instead, the rhombohedral samples possess an additional electronic polarizability, which is attributed to a change in bonding. Yet, we still need to explore how this change of bonding is related to changes of atomic arrangement, i.e. the crystallographic structure. This is depicted in the supplement, where both XRD and Raman spectra are displayed (**Fig. S2** and **Fig. S5**).

As shown there, the sudden drop in electronic polarizability is also accompanied by the transition from the rhombohedral to the hexagonal phase, with a concomitant change of the vibrational properties (as seen in the corresponding Raman spectra). The atomic arrangement hence differs significantly for the three crystallographic phases.

To establish that this discontinuity of the electronic polarizability between metavalent and covalent bonding in the GeTe-GeSe system is a more generic feature, the pseudo-binary lines from Sb_2Te_3 to Sb_2Se_3 and from Bi_2Se_3 to Sb_2Se_3 have been studied, too. Sb_2Te_3 is a prominent constituent of many phase-change materials, exhibits good thermoelectric properties[25], and shows properties typical for topological insulators.[26] Sb_2Te_3 also has the characteristic features of MVB such as a high

value for ε_∞ [27] and a slightly distorted octahedral arrangement.[7, 28] By contrast, Sb_2Se_3 features an orthorhombic atomic arrangement (*cf.* **Fig. S6** in the supplement), comparable to GeSe.[29] This crystalline compound is characterized by a small value of ε_∞, which is barely larger than the value found in the amorphous phase. Hence, in this material no metavalent bonds are formed.[7] This is in line with a previous theoretical study, which found the nearest-neighbour bonds in orthorhombic GeSe and Sb_2Se_3 to be stiff, strong, and covalent in their behaviour.[30] Thus, both lack the typical fingerprints of metavalently bonded materials. Therefore, the pseudo-binary line from Sb_2Te_3 to Sb_2Se_3 also allows to investigate how MVB collapses. As discussed for the GeTe-GeSe system, we observe a good miscibility of Sb_2Te_3 and Sb_2Se_3, as evidenced by the steady shift of XRD reflection positions with composition (*cf.* **Fig. S6 and S7** in the supplement). The comprehensive changes of XRD patterns, XRR densities (*cf.* **Fig. S8** in the supplement) and Raman spectra (*cf.* **Fig. S9** in the supplement) upon alloying Sb_2Te_3 with Sb_2Se_3 are presented and discussed in the supplement. **Fig. 3** displays the optical dielectric constant for various $Sb_2Se_{3x}Te_{3(1-x)}$ compounds.

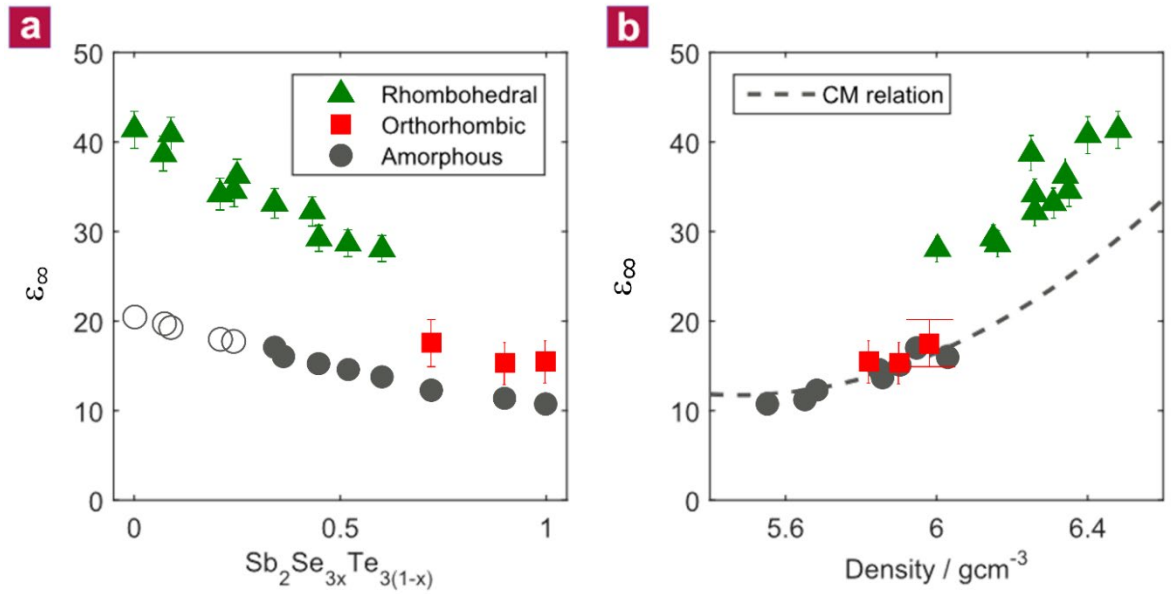

Fig. 3: Optical dielectric constant ε_∞ along the pseudo-binary line between Sb_2Te_3 and Sb_2Se_3: a) ε_∞ as a function of stoichiometry. As for the $GeTe_{1-x}Se_x$ system, the optical dielectric constant ε_∞ of the crystalline phase is much higher than the corresponding amorphous state. The transition from the rhombohedral to the orthorhombic phase is accompanied by an abrupt drop in ε_∞, indicative of a sudden breakdown of metavalent bonding. Samples with an Sb_2Se_3 content of less than 30% are already (partially) crystalline after deposition. Hence values for ε_∞ of these amorphous samples were extrapolated (open circles). **b)** The Clausius-Mossotti plot of ε_∞ versus the mass density confirms that the rapid drop of ε_∞ is not caused by a change of the mass density.

Again, two findings are noteworthy. A pronounced difference between the amorphous and crystalline phase is only observed for the Te-rich, rhombohedral phase. Upon the transition from the rhombohedral to the orthorhombic crystalline phase, a sudden drop in ε_∞ is found. XRR measurements were performed to confirm that this jump of ε_∞ at the transition is not due to a discontinuous change of the mass density. The density was found to decrease smoothly moving towards Sb_2Se_3 (see supplement). The optical dielectric constants are displayed in **Fig. 3b** as a function of the density. All iono-covalent compounds can be described well by the Clausius-Mossotti relation with a single set of bond polarizabilities (dashed line) as depicted in **Fig. 2**. Yet, this relation fails to describe the Sb_2Te_3-rich materials that develop MVB. As for the GeTe-GeSe line, the rhombohedral samples of $Sb_2Se_{3x}Te_{3(1-x)}$ possess an additional polarizability that arises from the creation of metavalent bonds upon crystallization. Hence, for both pseudo-binary lines, where substitutions were made on the anion sublattice, a sudden change of the optical dielectric constant ε_∞ is observed, which is indicative of a discontinuous change in bonding.

Yet, the Raman spectra depicted in the supplement also reveal that the atomic arrangement changes suddenly at the transition. Hence, from these results alone, it is not obvious if the discontinuous changes depicted in **Fig. 2** and **3** are caused by differences in atomic arrangement, differences in bonding or both. However, further data presented below provide a clear answer. The change of the vibrational properties can also be observed in FTIR spectra recorded in the far-infrared down to 20 cm^{-1} (2.5 meV). This is displayed in **Fig. 4**, where a striking difference in the frequency and intensity of the phonon modes is shown.

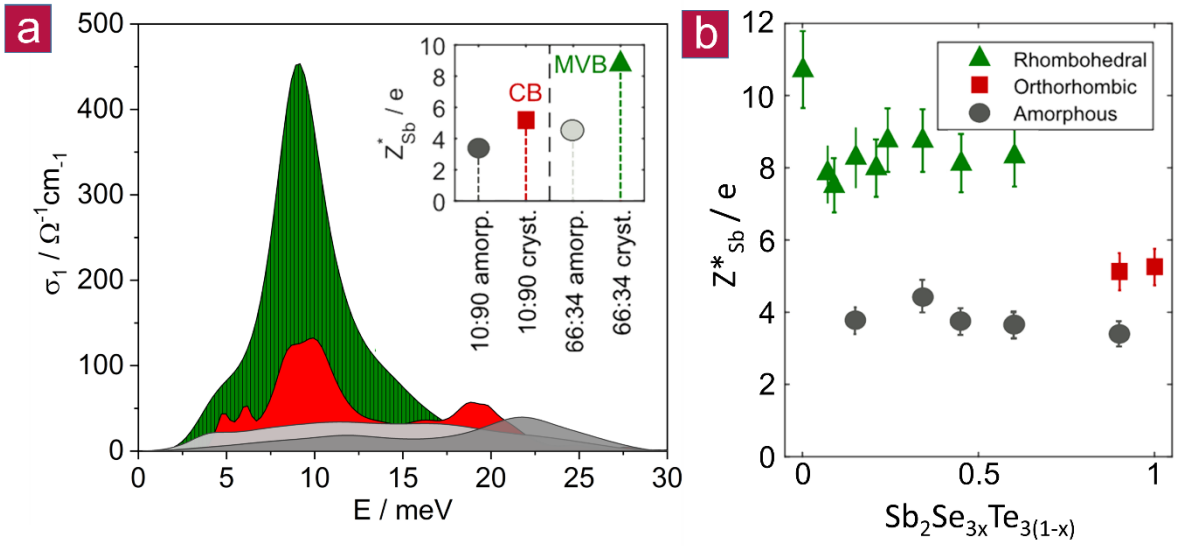

Fig. 4: Born-effective charge (Z*) of different $Sb_2Se_{3x}Te_{3(1-x)}$ compounds: a), Optical conductivity σ_1 of four different samples up to 40 meV, the range typical for optical phonons in higher chalcogenides. The integral of the curves represents the phonon spectral weight, which is linked to the Born-effective charge (Z*) (see supplement). The spectral weights of the amorphous phases of $Sb_2Se_{1.98}Te_{1.02}$ (shown in light gray and denoted as 66:34) and $Sb_2Se_{2.7}Te_{0.3}$ (dark gray, 90:10) do not differ significantly. Upon crystallization, a major increase of spectral weight is only found for $Sb_2Se_{1.98}Te_{1.02}$. This pronounced increase is directly related to a concomitant increase of the Born-effective charge (Z*). Note that the electronic background was subtracted for the conducting samples. **b),** Born-effective charge (Z*) for Sb in $Sb_2Se_{3x}Te_{3(1-x)}$. For all amorphous phases, values of Z^*_{Sb} around 4 are observed, independent of stoichiometry. The orthorhombic samples only show a slight increase of Z^*_{Sb} upon crystallization. On the contrary, the rhombohedral compounds are characterized by significantly higher values of 8-10. The simultaneous increase of Z^*_{Sb} and ε_∞ upon the formation of the rhombohedral phase is clear evidence for metavalent bonding and can be used as a fingerprint for its identification.

The rhombohedral samples show significantly stronger phonon modes, which can be ascribed to the high value of the Born effective charge (Z*), which characterizes the chemical bond polarizability in these compounds.[20] A large increase of Z* upon crystallization is observed for all rhombohedral compounds. This is different in the orthorhombic systems where only a small increase of Z* can be observed. Hence, the extraordinarily high values for Z* in the rhombohedral phase and the sudden drop upon the transition to the orthorhombic phase provide further evidence that the rhombohedral phase is governed by MVB in contrast to the conventional iono-covalent bonding in the orthorhombic materials.

Finally, we have investigated a third pseudo-binary line, i.e. Bi_2Se_3 – Sb_2Se_3. The corresponding data are presented and discussed in the supplement (*cf.* **Fig. S11 – S16**). Here, again a similar scenario unfolds upon replacing Bi by Sb. It is noteworthy, that MVB collapses regardless of whether substitutions are made on the cation or anion sublattice. The optical dielectric constant decreases significantly and the Raman spectra show a distinct change going from rhombohedral Bi_2Se_3 to orthorhombic Sb_2Se_3. These changes are accompanied by changes in the XRD patterns, indicative of distinct differences in atomic arrangement. A slight compositional broadening of the transition was found due to the miscibility gap in the Bi_2Se_3 – Sb_2Se_3 phase diagram. Interestingly, such miscibility gaps are often observed in phase diagrams when very similar chalcogenides are mixed, which employ different bonding mechanisms (i.e. metavalent and covalent bonding).

From these three cases, we can conclude that the collapse of metavalent bonding is accompanied by a sudden drop of the optical dielectric constant ε_∞ and the Born effective charge (Z*). To confirm that the discontinuous property changes are indeed due to changes in bonding, systematic studies of bond breaking for the GeTe – GeSe pseudo-binary have been performed using atom probe tomography (APT), as depicted in **Fig. S17 and Fig. S18**. A detailed discussion concerning APT and bond breaking can be found in the supplement and in previous publications.[6, 21] Our data show that the transition from rhombohedral $GeTe_{1-x}Se_x$ to hexagonal $GeTe_{1-x}Se_x$ and orthorhombic GeSe is accompanied by a discontinuous change in the probability of multiple events (i.e. bond breaking). While the latter two phases show a bond breaking pattern, which closely resembles the one for covalent bonding, the rhombohedral phase of $GeTe_{1-x}Se_x$ is characterized by an unconventional bond rupture, where each successful laser pulse dislodges several fragments with a high probability. Since atom probe tomography probes bond breaking rather than differences in atomic arrangement, this difference in bond rupture must be related to differences in bonding.[6] The discontinuous change of the optical dielectric constants upon the transition from the rhombohedral to the hexagonal/orthorhombic phase thus indeed coincides with a change of bond type.

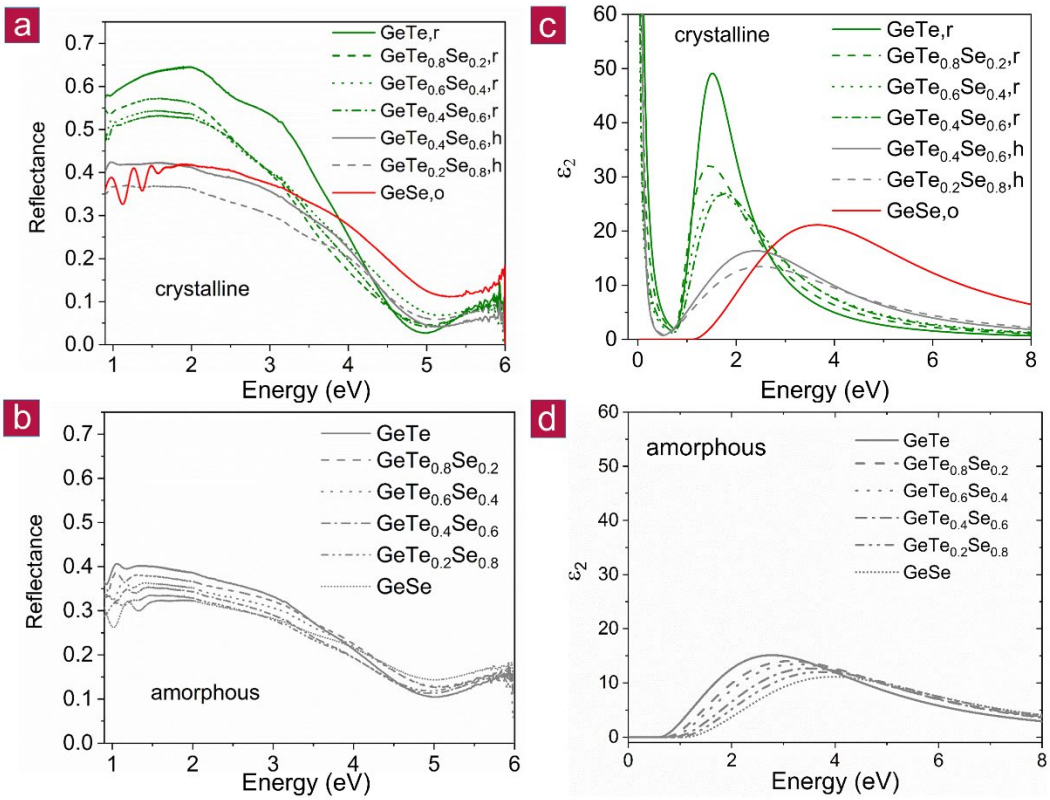

Fig. 5: Reflectance data for a) crystalline and b) amorphous $GeTe_{1-x}Se_x$ as well as the resulting imaginary part of the dielectric function $\varepsilon_2(\omega)$ of c) crystalline and d) amorphous $GeTe_{1-x}Se_x$: For the amorphous $GeTe_{1-x}Se_x$ series only very small continuous changes are observed upon increasing Se content for the reflectance. On the contrary, pronounced changes and a discontinuous jump in the reflectance are observed for crystalline $GeTe_{1-x}Se_x$. These changes can be attributed to changes in the imaginary part of the dielectric function $\varepsilon_2(\omega)$, in particular the height and position of its maximum. The pronounced and discontinuous change for the crystalline samples can be explained with the transition from metavalent to covalent bonding.

In the remainder of this paper, we will discuss what is the best way to describe and explain this change in chemical bonding. To this end, **Fig. 5** shows data obtained from optical spectroscopy. Details concerning data collection and fitting can be found in the experimental section and the supplementary information. In Fig. 5 a) and b), reflectance data are shown for amorphous and crystalline $GeTe_{1-x}Se_x$ from 1.1 eV to 5.9 eV. For the amorphous sample series only a modest and rather continuous change in reflectance is observed. For the crystalline sample on the contrary, the reflectance maxima are significantly decreasing in amplitude. Interestingly, the reflectance even decreases significantly upon the transition from the rhombohedral (r) to the hexagonal (h) phase of $GeTe_{1-x}Se_x$ compounds with

identical stoichiometry as exemplified for the $GeTe_{0.4}Se_{0.6}$ stoichiometry in **Fig. 5**. This implies that the corresponding valence and conduction band states, which determine the shape of the dielectric function (details can be found in the supplement) in the energy range up to 4 eV must change systematically with stoichiometry and structure. In contrast, much smaller changes occur for the amorphous series. This conclusion is supported by the imaginary parts of the dielectric functions (*cf.* Fig. 5c and d), which fit the measured optical data. For the crystalline series a significant decrease of the height of the maximum of $\varepsilon_2(\omega)$ is found upon increasing Se content, accompanied by a concomitant increase of the position of this maximum. Especially noteworthy is the drop of the height of the maximum of $\varepsilon_2(\omega)$ for crystalline samples with identical stoichiometry but different atomic arrangement. On the contrary, for the amorphous series only a marginal change of the imaginary part of the dielectric function is observed. This indicates that there are much more pronounced changes in the nature of the valence and conduction band states for the crystalline than the amorphous sample series. The occupied and empty states directly below and above the Fermi level are predominantly attributed to p-electrons, which form σ-bonds (*cf.* **Fig. 6**).[3, 31]

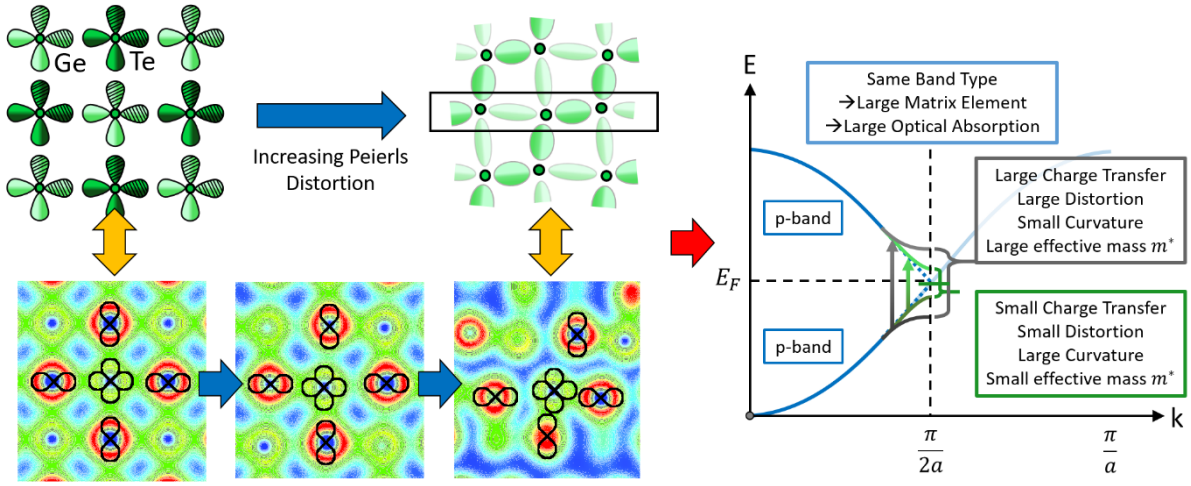

Fig. 6: Illustration of the bond formation in GeTe and the resulting band structure: Atomic orbitals of Ge and Te responsible for bond formation in GeTe are depicted on the left. σ-bonds are formed from p-orbitals, which are occupied by about half an electron pair (ES ≈ 1), resulting in a metallic band (blue curves on the right side of the figure). However, moderate charge transfer and significant electron sharing result in a small bandgap. When alloying GeTe with Se, the degree of electron sharing significantly increases (*cf.* **Fig. 1**), resulting in an increased Peierls distortion, which can be verified experimentally (*cf.* **Fig. 5**). Figure adapted from Ref. [32]. On the bottom, from left to right, valence charge density plots for GeTe in the cubic, rhombohedral (equilibrium) and orthorhombic

phases. The central atom is Ge. Same color scale ranges and isolines values for all phases. The alignment of the p orbitals and extent of the Peierls distortion is linked to the existence of MVB. In the orthorhombic phase, the loss of orbital alignment and large Peierls distortion ratios in the y direction of the figure is triggering the disappearance of MVB. The projection plane is defined by a Ge-Te-Te triplet of atoms (other atoms are thus out of-plane for the rhombohedral and orthorhombic phases).

All materials studied here are isoelectronic to GeTe, i.e. they have on average 3 p-electrons per lattice site. GeTe and all other compounds on the pseudo-binary line between GeTe and GeSe have 6 valence p-electrons, which form σ–bonds. For an octahedral arrangement, these p-orbitals are perfectly aligned. In this case there is only a small band gap due to the modest charge transfer between Ge and Te as already previously noted. Yet, this situation has a pronounced consequence for the matrix element for the optical transition. The perfect octahedral arrangement leads to a large overlap of the wave functions of the initial and final state and hence a large matrix element for the optical transition. This is depicted in **Fig. 7**.

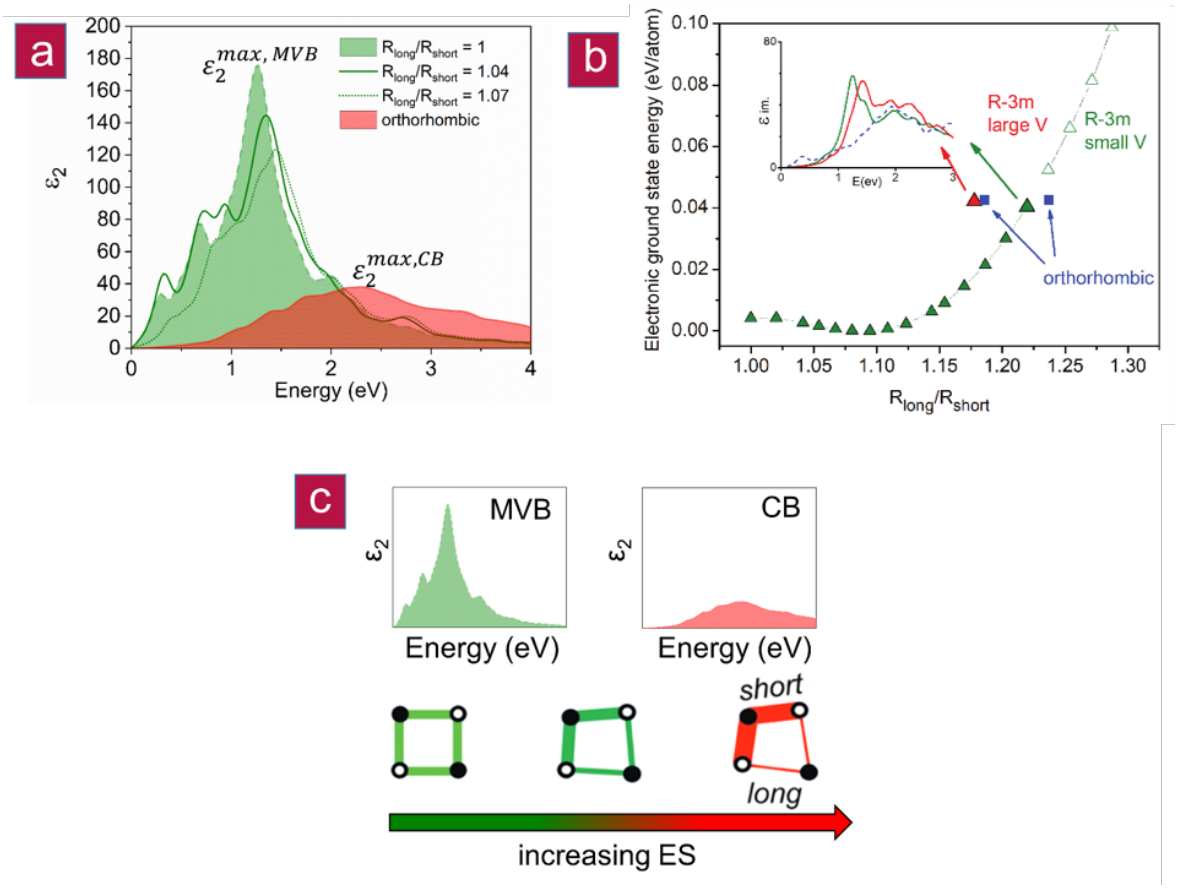

Fig. 7: Theoretical $\varepsilon_2(\omega)$ as a function of the Peierls Distortion (i.e. R_{long}/R_{short}): a) shows the optical absorption ($\varepsilon_2(\omega)$) as a function of the degree of the R_{long}/R_{short} ratio for rhombohedral GeTe (green) and orthorhombic GeTe (red), confirming the experimental findings of a discontinuous transition from MVB to CB; **b)** electronic ground state energy as a function of the R_{long}/R_{short} ratio. The optimized orthorhombic phase is anisotropic, with two different Peierls distortion ratios. At comparable cohesive energy, once can find two rhombohedral phases with different volumes (larger triangles). These rhombohedral phases differ by less than 2 meV/atom in energy, but vary by more than 5% in volume, an absorption peak shifted by about 0.2eV (inset) and a decreased dielectric constant for the larger volume structure. **c)** shows a scheme demonstrating the effect of increasing ES on the R_{long}/R_{short} ratio and on $\varepsilon_2(\omega)$. These findings confirm the discontinuous character of the MVB-CB border.

In GeTe, the large values of ε_2^{max} has been attributed to the alignment of the p-orbitals of adjacent atoms, i.e. a weak Peierls distortion.[32-33] For the $GeTe_{1-x}Se_x$ series (*cf.* **Fig 5**), a decreasing amplitude and increasing energy of ε_2^{max} is observed. This finding can be reproduced, if we calculate the optical properties of crystalline GeTe as a function of an increasing Peierls distortion (i.e. the R_{long}/R_{short} ratio), which also decreases the p-orbital alignment (*cf.* **Fig 7**). The increasing Peierls distortion leads to an increase of charge accumulation in the shorter bonds [34]. The concomitant decrease in p-orbital alignment is visible in the changes of the matrix element shown in **Fig. 8.** For R_{long}/R_{short} ratios in the range from 1.15 to 1.20, several structures are energetically almost identical, yet have different atomic densities and symmetries. This can explain the abrupt change in properties measured for the $GeTe_{1-x}Se_x$ series. Upon increasing the Peierls distortion, the number of electrons shared between adjacent atoms increases, while the effective coordination number decreases. The number of electrons transferred between Ge and Te is almost not altered. Hence, **Fig. 7** shows the impact of the Peierls distortion (i.e. changes in ES alone) on ε_2^{max}. These findings confirm that an increasing Peierls distortion decreases the magnitude and increases the energy of ε_2^{max} and that the transition from metavalent to covalent bonding is discontinuous, strengthening our hypothesis that the metavalent bond is a new, fundamental bonding type in solids. This is also confirmed by results shown in **Fig. 8**, where the matrix element (ME) and the joint density of states (JDOS) are shown for different degrees of Peierls distortion. Clear differences in the matrix element are visible when comparing MVB (*cf.* **Fig. 8 a and b**) and CB (*cf.* **Fig. 8 c and d**), i.e. p-orbital overlap is distinctly different. It is noteworthy that changes in the joint density of states are subtle compared to changes in the matrix element, i.e. the changes in optical absorption shown in **Fig. 7** are predominantly governed by chemical bonding.

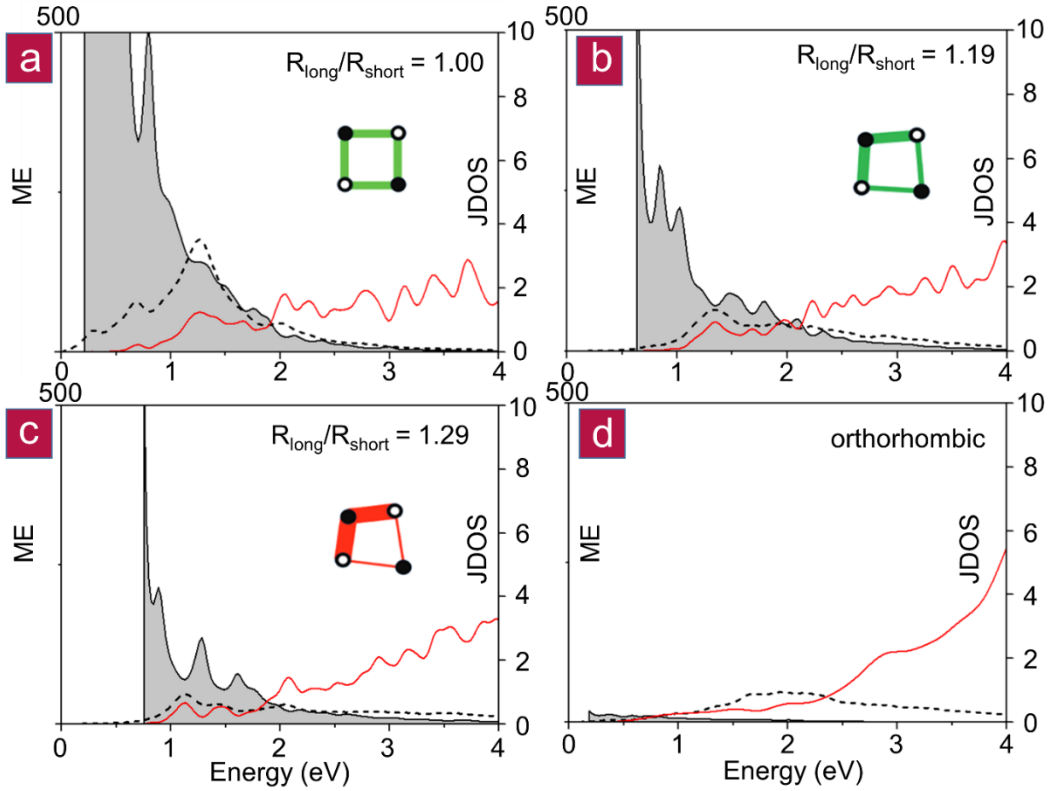

Fig. 8: Matrix element (ME) and joint density of states (JDOS): An increase in ES (i.e. in R_{long}/R_{short}) results in significant changes in the matrix element (i.e. in p-orbital overlap) shown in grey, while the joint density (red curves) remain similar within the same crystal system. This figure shows clear differences between metavalent (a and b) and covalent (c and d) systems. $\varepsilon_2(\omega)$ is shown as black dotted lines.

Hence, this work demonstrates that chemical bonding in solids can be controlled by both the strength of the Peierls distortion (i.e. the R_{long}/R_{short} ratio) and the concomitant p-orbital alignment, which can be described by the chemical bond descriptor ES. However, chemical bonding can also be controlled by the charge transfer between adjacent atoms in a perfect octahedral atomic arrangement, characterized by the chemical bond descriptor ET.[32] For PbX (X = Te, Se, S), there is no Peierls distortion and all three higher lead mono chalcogenides crystallize in the rocksalt structure, i.e. a perfect octahedral arrangement. These lead chalcogenides show an increasing electron transfer (ET) from PbTe, to PbSe and finally PbS, which causes a decrease of the amplitude and an increase of the energy of ε_2^{max}, related to changes in the matrix element.[32] The number of electrons shared (ES) and the electron transfer (ET) between adjacent atoms can therefore be viewed as the natural variables to describe chemical bonding in solids.

Regarding the starting hypothesis of this work, the answer is clear. Our findings demonstrate unequivocally that there is a distinct border between metavalent and covalent bonding (*cf.* **Fig. 1**), regardless whether substitution is performed on the (formal) anion or cation sublattice. This inference immediately raises several interesting questions: Is there a link between metavalent bonding in solids and unconventional bonding mechanisms reported for molecules? Heated debates about the nature of chemical bonds have accompanied the development of quantum mechanics [35] [36] . Initially, the discussions focused on bonding in molecules. In recent decades, compelling evidence has been presented for unconventional bonding mechanisms in molecules where concepts such as charge shift bonding [37], hypervalent bonding [38]or 3 center – 2 electron (3c – 2e) bonding [39] have been proposed. It is hence interesting to look for similarities between metavalent bonding in solids and these unconventional bonds in molecules. However, it is also obvious that MVB differs significantly from those molecular bonds. So far, to our knowledge, these unconventional molecular bonds have not been related to unique measurable properties of molecules, while the concepts presented here have been developed to provide new design strategies for solids. Furthermore, the unconventional bonds in molecules are usually discussed as a sub-group of covalent bonds. A discontinuous transition between e.g. covalent bonding and charge-shift bonding, for example, has not been reported to our knowledge, while compelling evidence has been presented demonstrating the discontinuous nature of the transition between metavalent and covalent bonding in solids. This transition raises further interesting questions and provides opportunities for systematic materials design. One can wonder, for example, how the border between metavalent and metallic bonding as well as ionic bonding[32] looks like? Metavalent bonding is characterized by the competition between electron delocalization (as in metallic bonding) and electron localization (as in ionic and covalent bonding). Further support for this claim comes from transport data summarized in **Fig. 9** for the $Sb_2Se_{3x}Te_{3(1-x)}$ system, which reveal that the room temperature conductivity of the metavalently bonded materials in this series are all located in a narrow range of about $10^{3\pm1}$ S/cm, while the covalently bonded materials have a significantly lower electrical conductivity at room temperature.

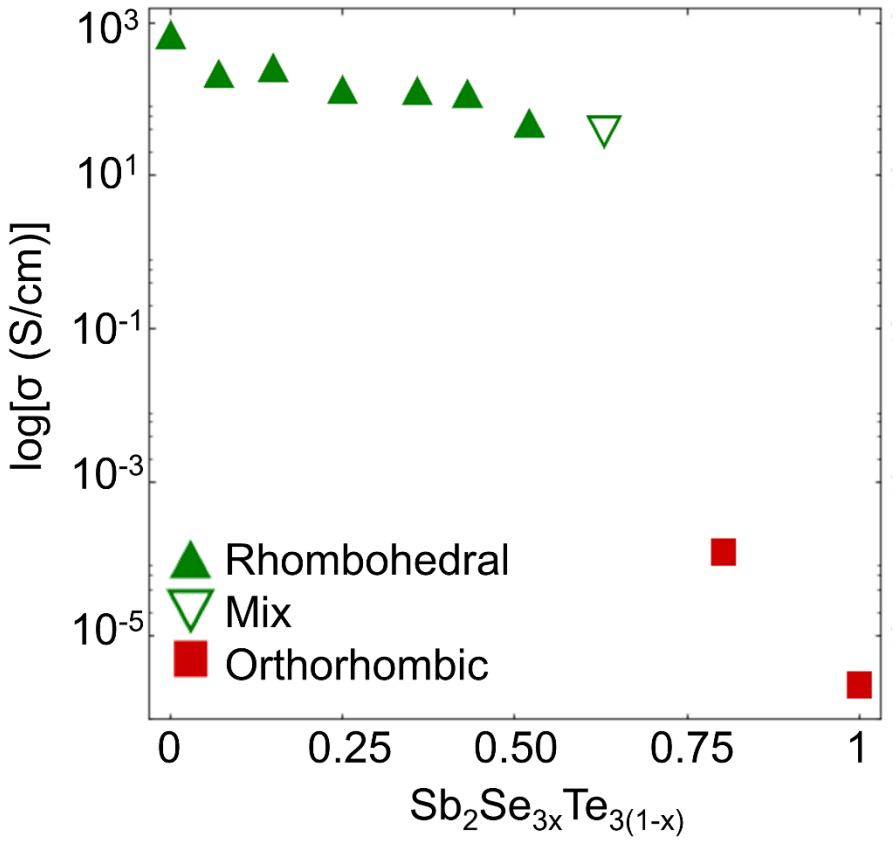

Fig. 9: Electrical conductivity of $Sb_2Se_{3x}Te_{3(1-x)}$ system: At the border between metavalent and covalent bonding the electrical conductivity drops by several orders of magnitude, indicative of a strong increase in charge carrier localization.

Once the system transitions from metavalent to covalent, the electrical conductivity sharply decreases by 4-6 orders of magnitude. Hence, a low temperature transition from insulating to metallic behavior can be expected, if the border between metavalent and metallic bonding is crossed. For these materials electron correlations are weak, since the static dielectric constant is very large.[40] Hence, this border provides the fascinating opportunity to investigate the nature of the metal-insulator transition without pronounced electron correlation.

Exploring the borders of metavalent bonding is not only interesting for fundamental questions related to the nature of chemical bonding in solids and its relationship to characteristic properties. It also provides a clear understanding for which range of materials a portfolio of attractive properties for specific applications can be expected. One example is the recent investigation of In_3SbTe_2 for photonic

applications in the NIR, which demonstrates the potential of such materials. In_3SbTe_2 shows the characteristic property portfolio of phase change materials. There is for example a significant change of optical properties upon crystallizing this compound. While amorphous samples show the characteristic features of covalently bonded materials, the crystalline phase has a high electrical conductivity and shows a Drude-like reflectance in the NIR.[41] In the map of **Fig. 1**, this material has an ES value which locates this material below the dashed line, which is apparently the borderline for MVB compounds. Below this line, unconventional metals are found. Typical phase change materials like GeTe and $Ge_2Sb_2Te_5$, on the contrary are characterized by larger ES values. Hence, one can ponder if the map in figure 1 can be employed to tailor phase change materials. This question was recently answered in the affirmative[42]. By studying the effect of iso-electronic element replacement, i.e. replacing Te by Se, or replacing Ge by Sn the crystallization speed could be altered by a factor of 10^6! This pronounced change in kinetics can be attributed to significant changes of bonding.

Finally, it has recently been shown that good thermoelectrics based on mono-chalcogenides can be found for those materials, which possess the characteristics of metavalent bonding, while the covalently bonded materials showed a by far inferior performance.[14] [43] [44] The improvement of the thermoelectric properties can be partly attributed to an improvement of electronic properties, related to the unique band structure of the metavalently bonded materials, which leads to a sudden jump of the power factor upon the transition from covalent to metavalent bonding [43] [44]. Yet, also the thermal properties are superior for the metavalent solids, which are characterized by soft, anharmonic bonds, which reduce the thermal conductivity[45] [3]. The low frequency of transverse optical modes can be attributed to the fact that the longitudinal optical modes already have a relatively low frequency, since the bond order between adjacent atoms is ½ (ES ≈ 1) and the masses of the atoms involved are large. The transverse optical modes are even significantly lower in frequency, since the Born effective charges of the atoms are large [3], leading to a strong increase of the static dielectric constant ε_{st} over the optical dielectric constant ε_{∞} and hence low frequency transverse optical modes. This can be seen from the

Lydanne-Sachs-Teller relationship [46]which links the frequencies of transverse and longitudinal optical modes to the ratio of ε_∞ and ε_{st}.

In this context, the sharp transition from metavalent to covalent bonding discussed here as well as previous work on the transition between metavalent and iono-covalent bonding [32] provides a blueprint to tailor the property portfolio relevant for phase change materials and thermoelectrics based on the two natural variables for chemical bonding, the electrons shared and transferred between adjacent atoms.

Experimental Methods

Sample preparation

To prepare FTIR samples, a 150 nm Al layer is deposited onto a glass substrate. Alternatively, Si<100> was used as a substrate. Subsequently, the films to be investigated (thickness 400 – 800 nm) are deposited. DC and RF magnetron sputtering is used for film deposition (background pressure 2 x 10^{-6} mbar, 20 sccm argon as sputter gas). Stoichiometric targets of Al, GeTe, GeSe, Sb_2Te_3, Sb_2Se_3 and Bi_2Se_3 and $(ZnS)_{80}$:$(SiO_2)_{20}$ (purity 99.99 %) were used as sputter targets. To adjust the stoichiometry, the sputter power of the corresponding targets is adjusted. Films for far-infrared FTIR measurements have been prepared on double-side polished Si <100> substrates (ρ > 5000 mΩcm) that have subsequently been cleaned in acetone, isopropanol and distilled water within an ultrasonic bath. Raman samples have been prepared on boron-doped, single-side polished Si <100> substrates. Ellipsometry and reflectance samples have been prepared on phosphorus-doped single-side polished Si <100> substrates and they have additionally been capped with 9 nm of $(ZnS)_{80}$:$(SiO_2)_{20}$ in order to mitigate evaporation of Se during crystallization. For all capped samples an additional reference sample with just the capping layer has been prepared during the same sputter run to estimate its influence on the measurements.

The as-deposited amorphous films were crystallized in an argon atmosphere. The film structure was verified by X-ray diffraction, while the film densities were determined using X-ray reflectivity measurements. The film thickness was determined on reference samples prepared in the same sputter session using a Bruker DekTak profilometer. Several thickness values were taken at different positions and their average values were used as a reference for the optical simulations.

Optical measurements

Reflectance measurements shown in Fig. 5 were performed in an Avantes AvaSpec-ULS2048CL-EVO spectrometer at normal incidence over a spectral range of 1.1 eV (9.100 cm^{-1}) to 5.9 eV (47.000 cm^{-1}) using an aluminum mirror as a reference. Measurements in the visible range (i.e. from 9.000 to 18.000 cm^{-1}) were performed using a Bruker Vertex 80v Fourier-transform spectrometer in order to increase

data quality. Reflectance spectra in the range from 50 meV (400 cm^{-1}) to 1 eV (8.000 cm^{-1}) have been measured, using a Bruker IFS 66v/s spectrometer with a resolution of 0.24 meV using a globar source. The reflectance spectra of an Al mirror reference and the sample were measured subsequently to exclude drift effects. For normalization, the final spectrum was obtained by dividing the measured spectrum by the reference. The angle of incidence of the incoming beam was kept constant at 10° with respect to the surface normal. The relative measurement error for the reflectance is 0.2% in the wavelength range measured.

Transmission data have been recorded from 2.5 meV (20 cm^{-1}) to 1.5 eV (12.000 cm^{-1}), the Si band gap prevented us to go higher. The response of the bare substrates has also been recorded. The data was collected in a Bruker IFS66/v spectrometer. In order to cover the whole spectral range, we utilized a 4K bolometer, far and mid infrared DLTGS detectors, a liquid nitrogen cooled InSb photoconductor and a Si photodiode in combination with Hg-arc, globar and tungsten lamps. Three beam splitters, Ge on Mylar, Ge on KBr, and Quartz, were utilized. As the films and substrate have optical quality parallel surfaces, Fabry-Pérot interferences are clearly discernible in our data. We chose a spectral resolution of 5 cm^{-1} which washes out the interference fringes of the substrate, while preserving phonon spectral signatures of the film. For an anisotropic system, the quantities ϵ_∞ and Z^* are described by tensors. However, the XRD measurements clearly reveal that all samples are polycrystalline and do not exhibit a pronounced texture. Hence, the measured values for ϵ_∞ and Z^* correspond to an average over all crystallographic orientations.

Raman measurements were carried out using a WITec alpha300 R confocal Raman microscope with a 532 nm laser. The measurements were performed at room temperature under ambient condition using a 50× objective. The resulting spot size was around 400 nm. All spectra were recorded using a grating with 1800 lines/mm and a resolution of around 1 cm^{-1}. Due to the low heat conductance and a low melting point of the films a laser power of 100 µW was employed. All measurements were taken at different spots on the sample to evaluate the spatial variation of the Raman signal.

To verify the stoichiometry, x-ray spectroscopy (EDX) was performed. A FEI Helios 650 NanoLab system was used to obtain the EDX data. The AZtec 2.1 software was employed for data analysis. The electron beam was operated at 10 keV and 0.4 nA on a 200 x 300 µm area and was calibrated with a copper sample prior to measurement.

Modelling of the spectra

The infrared response of a material is fully characterized by its frequency dependent dielectric function $\epsilon(\omega)$, which is a linear superposition of different excitations. For our materials we utilized:

$$\varepsilon(\omega) = \varepsilon_{const.} + \varepsilon(\omega)_{Drude} + \varepsilon(\omega)_{Tauc-Lorentz} + \sum \varepsilon\,(\omega)_{Lorentz} \qquad (1)$$

Besides a constant high frequency contribution, $\epsilon(\omega)$also has a Drude[47] term for mobile carriers; a Tauc-Lorentz [48] [49]model for the interband gap; and harmonic Lorentz oscillators[47] for localized polar excitations, such as phonons.

The reflectance spectra were analyzed in the range from 50 meV to 3 eV using the SCOUT software. A layer stack consisting of a thin film (500 nm – 800 nm)/Al mirror (150 nm)/glass substrate (500 µm) was simulated, with the dielectric function of aluminum taken from a database. The latter was checked to be in excellent agreement with the optical properties of a reference specimen, the Al coating. The film thickness of the semiconductor was fitted within the confidence interval of the DekTak profilometer. The optical dielectric constant was determined from the dielectric function as $\epsilon_\infty = \epsilon_1(0.05\ eV)$, after subtracting the Drude contribution, when necessary.

Transmission from 3 meV to 1.5 eV in thin films were analyzed with a custom-made software considering a thin film over silicon substrate stack. Coherent light propagation was assumed in the film and, because of the choice of spectral resolution, incoherent propagation in the substrate. Both bare substrate and stack were modeled with the dielectric function described above. This gives a very good but not perfect description of the system transmittance. However, tiny deviations between data and fit indicate that excitations in the film and, to a lesser extent also in the substrate, do not follow exactly the dielectric function models mentioned above. These models exclude, for instance, phonon anharmonic effects. A model independent refinement to the data can be achieved by a variational

correction to the dielectric function as proposed by Kuzmenko [50], which gives results with an accuracy equivalent to Kramers-Kronig. It is particularly useful for our data as the inversion of the transmission and its Kramers-Kronig calculated phase in multilayer systems is numerically unstable. Our implementation chosen for this variational approach is described in Ref. [51].

Computational details

All theoretical calculations in this paper were performed using Density Functional Theory as implemented in the *Vienna ab initio simulation package* (VASP)**.** [52] [53] [54] [55] The electronic structure was computed using PAW potentials [56] with Ge (4s,4p) and Te (5s, 5p) electrons treated as valence electrons. The exchange-correlation was computed using the PBEsol functional [57] and the plane waves basis was expanded up to a 520 eV kinetic energy cutoff. The Brillouin zone was sampled with 14 x 14 x 14 kpoints for the rhombohedral (*R-3m)* phase and 12 x 8 x 12 kpoints for the orthorhombic (*Pnma)* phase. The dielectric functions were computed using Fermi's golden rule and a sum over states close to the Fermi level (5/14 and 20/28 valence/conduction states for the *R-3m* and the *Pnma* phases, respectively). All structures have been relaxed (maximal residual force lower than 1E-4 eV/Å) keeping the following constraints. For the rhombohedral phase, the R_{long}/R_{short} ratio was imposed, whereas for the Pnma phase the atoms were only allowed to move along one of the cell vectors at once.

The total energy of the relaxed *Pnma* phase is 55 meV/atom higher than the equilibrium *R-3m* structure, and equal to the *R-3m* structure for which the Peierls distortion ratio is about 1.22.

Data availability

All data in this Article are available from the corresponding author upon reasonable request.

References

[1] M. Laing, *Journal of Chemical Education* **2008**, 85.
[2] L. J. Meyer, *Die modernen Theorien der Chemie und ihre Bedeutung für die chemische Statistik*, **1864**.
[3] B. J. Kooi, M. Wuttig, *Advanced Materials*, DOI: 10.1002/adma.2019083021908302.
[4] M. Wuttig, V. L. Deringer, X. Gonze, C. Bichara, J. Y. Raty, *Advanced Materials* **2018**, 30, 1803777.
[5] D. Giri, L. Williams, A. Mukherjee, K. Rajan, *Journal of Chemical Physics* **2021**, 154, 124105.
[6] M. Zhu, O. Cojocaru-Miredin, A. M. Mio, J. Keutgen, M. Kupers, Y. Yu, J. Y. Cho, R. Dronskowski, M. Wuttig, *Advanced Materials* **2018**, 30, 1706735.
[7] Y. D. Cheng, O. Cojocaru-Miredin, J. Keutgen, Y. Yu, M. Kupers, M. Schumacher, P. Golub, J. Y. Raty, R. Dronskowski, M. Wuttig, *Advanced Materials* **2019**, 31, 1904316.
[8] M. Wuttig, V. L. Deringer, X. Gonze, C. Bichara, J. Y. Raty, *Advanced Materials* **2018**, 30, 1803777.
[9] S. Maier, S. Steinberg, Y. Cheng, C.-F. Schön, M. Schumacher, R. Mazzarello, P. Golub, R. Nelson, O. Cojocaru-Mirédin, J.-Y. Raty, M. Wuttig, *Advanced Materials* **2020**, 32, 2005533.
[10] J. Y. Raty, M. Schumacher, P. Golub, V. L. Deringer, C. Gatti, M. Wuttig, *Advanced Materials* **2019**, 31, 1806280.
[11] V. P. Cuenca-Gotor, J. A. Sans, O. Gomis, A. Mujica, S. Radescu, A. Munoz, P. Rodriguez-Hernandez, E. L. da Silva, C. Popescu, J. Ibanez, R. Vilaplana, F. J. Manjon, *Physical Chemistry Chemical Physics* **2020**, 22.
[12] M. Xu, S. Jakobs, R. Mazzarello, J. Y. Cho, Z. Yang, H. Hollermann, D. S. Shang, X. S. Miao, Z. H. Yu, L. Wang, M. Wuttig, *Journal of Physical Chemistry C* **2017**, 121.
[13] M. Wuttig, C.-F. Schoen, M. Schumacher, J. Robertson, P. Golub, E. Bousquet, J.-Y. Raty, **2020**, arXiv:2012.03794.
[14] D. Sarkar, S. Roychowdhury, R. Arora, T. Ghosh, A. Vasdev, B. Joseph, G. Sheet, U. V. Waghmare, K. Biswas, *Angew Chem Int Ed Engl* **2021**, DOI: 10.1002/anie.202101283.
[15] R. Bader, T. Nguyen-Dang, in *Advances in Quantum Chemistry*, Vol. 14, Elsevier **1981**, p. 63-124.
[16] R. F. W. Bader, *Accounts of Chemical Research* **1985**, 18.
[17] R. F. W. Bader, M. E. Stephens, *Journal of the American Chemical Society* **1975**, 97.
[18] G. N. Lewis, *Valence and the structure of atoms and molecules*, University Microfilms, Ann Arbor, Mich. **1977**.
[19] L. L. Zhao, W. H. E. Schwarz, G. Frenking, *Nature Reviews Chemistry* **2019**, 3.
[20] X. Gonze, C. Lee, *Physical Review B* **1997**, 55.
[21] S. Maier, S. Steinberg, Y. D. Cheng, C. F. Schon, M. Schumacher, R. Mazzarello, P. Golub, R. Nelson, O. Cojocaru-Miredin, J. Y. Raty, M. Wuttig, *Advanced Materials* **2020**, 32, 2005533.
[22] J. A. Muir, R. J. Cashman, *Journal of Physics and Chemistry of Solids* **1967**, 28.
[23] H. Wiedemeier, P. A. Siemers, *High Temperature Science* **1984**, 17.
[24] E. Talebian, M. Talebian, *Optik* **2013**, 124.
[25] B. Fang, Z. G. Zeng, X. X. Yan, Z. Y. Hu, *Journal of Materials Science-Materials in Electronics* **2013**, 24.
[26] H. J. Zhang, C. X. Liu, X. L. Qi, X. Dai, Z. Fang, S. C. Zhang, *Nature Physics* **2009**, 5.
[27] S. Liu, J. S. Wei, F. X. Gan, *Applied Physics Letters* **2012**, 100, 111903.
[28] J. L. F. Da Silva, A. Walsh, H. L. Lee, *Physical Review B* **2008**, 78, 224111.
[29] N. W. Tideswell, F. H. Kruse, J. D. McCullough, *Acta Crystallographica* **1957**, 10.
[30] V. L. Deringer, R. P. Stoffel, M. Wuttig, R. Dronskowski, *Chemical Science* **2015**, 6.
[31] D. Lencer, M. Salinga, M. Wuttig, *Advanced Materials* **2011**, 23.
[32] S. Maier, S. Steinberg, Y. Cheng, C.-F. Schön, M. Schumacher, R. Mazzarello, P. Golub, R. Nelson, O. Cojocaru-Mirédin, J.-Y. Raty, M. Wuttig, **2020**, 32.
[33] B. Huang, J. Robertson, *Physical Review B* **2010**, 81, 081204.

[34] J. Y. Raty, M. Wuttig, *Journal of Physics D-Applied Physics* **2020**, 53, 234002.
[35] L.Pauling, *The Nature Of The Chemical Bond*, Cornell University Press, **1960**.
[36] K. Gavroglu, A. Simões, *Neither Physics nor Chemistry: A History of Quantum Chemistry*, MIT Press, London **2012**.
[37] S. Shaik, D. Danovich, J. M. Galbraith, B. Braida, W. Wu, P. C. Hiberty, *Angewandte Chemie-International Edition* **2020**, 59.
[38] V. I. Minkin, *Pure and Applied Chemistry* **1999**, 71.
[39] J. C. Green, M. L. H. Green, G. Parkin, *Chemical Communications* **2012**, 48.
[40] T. Siegrist, P. Jost, H. Volker, M. Woda, P. Merkelbach, C. Schlockermann, M. Wuttig, *Nature Materials* **2011**, 10.
[41] A. Hessler, S. Wahl, T. Leuteritz, A. Antonopoulos, C. Stergianou, C. F. Schon, L. Naumann, N. Eicker, M. Lewin, T. W. W. Mass, M. Wuttig, S. Linden, T. Taubner, *Nature Communications* **2021**, 12, 924.
[42] C. Persch, M. J. Müller, A. Yadav, J. Pries, N. Honné, P. Kerres, S. Wei, H. Tanaka, P. Fantini, E. Varesi, F. Pellizzer, M. Wuttig, 2021, arXiv:2103.00116.
[43] Y. Yu, M. Cagnoni, O. Cojocaru-Miredin, M. Wuttig, *Advanced Functional Materials* **2019**, 30, 1904862.
[44] M. Cagnoni, D. Fuhren, M. Wuttig, *Advanced Materials* **2018**, 30, 1801787.
[45] T. Matsunaga, N. Yamada, R. Kojima, S. Shamoto, M. Sato, H. Tanida, T. Uruga, S. Kohara, M. Takata, P. Zalden, G. Bruns, I. Sergueev, H. C. Wille, R. P. Hermann, M. Wuttig, *Advanced Functional Materials* **2011**, 21.
[46] R. H. Lyddane, R.G. Sachs, E. Teller, *Physical Review* **1941**, 59.
[47] F. Wooten, *Optical Properties of Solids*, Academic Press, INC, New York **1972**.
[48] W.J.Potts, *Wiley* **1963**.
[49] M. Schubert, in *Infrared Ellipsometry on Semiconductor Layer Structures: Phonons, Plasmons, and Polaritons*, Vol. 209, Springer-Verlag Berlin, Berlin **2004**, p. 1-6.
[50] A. B. Kuzmenko, *Review of Scientific Instruments* **2005**, 76, 083108.
[51] G. Chanda, R. Lobo, E. Schachinger, J. Wosnitza, M. Naito, A. V. Pronin, *Physical Review B* **2014**, 90, 024503.
[52] G. Kresse, J. Furthmuller, *Computational Materials Science* **1996**, 6, 15.
[53] G. Kresse, J. Furthmüller, *Phys. Rev. B: Condens. Matter Mater. Phys.* **1996**, 54, 15.
[54] G. Kresse, D. Joubert, *Physical Review B* **1999**, 59, 1758.
[55] G. Kresse, J. Furthmuller, J. Hafner, *Physical Review B* **1994**, 50, 13181.
[56] P. E. Blochl, *Physical Review B* **1994**, 50, 17953.
[57] J. P. Perdew, A. Ruzsinszky, G. I. Csonka, O. A. Vydrov, G. E. Scuseria, L. A. Constantin, X. L. Zhou, K. Burke, *Physical Review Letters* **2008**, 100, 136406.

Author Contributions:

L.G., S.J. and A. v. H. produced most samples and characterized them by XRD, XRR and FTIR. A.P. and A.P. studied GeSe, S. J. and A. v. H. studied the GeTe-GeSe and Sb_2Te_3-Sb_2Se_3 series, while L. G. and S. M. studied the Bi_2Se_3-Sb_2Se_3 series. Data for Fig. 5 were produced by C. T., S. W. and Y. Z. R.P.S.M.L. characterized the low frequency FTIR spectra and M. R. and M.D. measured the Raman spectra. J.Y.R. produced and analyzed the ab initio simulation data. The paper was written by L. G., S. J., S. M. and M. W., with the help and through contributions from all co-authors. All authors have given approval to the final version of the manuscript. The project was initiated and conceptualized by M.W.

Notes

The authors declare no competing financial and/or conflict of interest.

Acknowledgement

We thank K. Shportko for FTIR measurements, and M. Wirtssohn for carrying out EDX measurements, both focusing on the GeTe – GeSe pseudo-binary line. H. Volker and V. Deringer (Oxford) are gratefully acknowledged for careful reading of the manuscript and W. Sander (RU Bochum) is gratefully acknowledged for helpful discussions on resonance bonding or the lack thereof in aromatic compounds. This work was partially supported through the SFB 917 (Nanoswitches). M.W. furthermore acknowledges funding by an ERC Advanced Grant 340698 (‘Disorder control’) and a Distinguished Professorship. S.M. gratefully acknowledges financial support from the ERS Start-Up grant for postdocs 2018 (grant number: StUpPD_324-18), while J.-Y. R. acknowledge support from the FRS-FNRS (CDR grant ABIGLO J.0154.21), and the CÉCI (funded by the F.R.S.-FNRS under Grant No. 2.5020.11) and the Tier-1 supercomputer of the Fédération Wallonie-Bruxelles (grant n°1117545).

Supplement: Metavalent bonding in crystalline solids: how does it collapse?

L. Guarneri[1,*], S. Jakobs[1,*], A. von Hoegen[1,*], S. Maier[1], M. Xu[1], M. Zhu[1], S. Wahl[1], C. Teichrib[1], Y. Zhou[1], O. Cojocaru-Mirédin[1], M. Raghuwanshi[1], C.-F. Schön[1], M. Drögeler[2], C. Stampfer[2,3], R. P. S. M. Lobo[4a,4b], A. Piarristeguy[5], A. Pradel[5], J.-Y. Raty[6], M. Wuttig[1,3,7]

[1] RWTH Aachen University, I. Physikalisches Institut (IA), 52056 Aachen, Germany

[2] RWTH Aachen University, II. Physikalisches Institut (IIA), 52056 Aachen, Germany

[3] JARA-FIT and JARA-HPC, RWTH Aachen University, 52056 Aachen, Germany

[4a] LPEM, ESPCI Paris, CNRS, PSL University; 10 rue Vauquelin, F-75005 Paris, France

[4b] Sorbonne Université, ESPCI Paris, CNRS, LPEM, F-75005 Paris, France

[5] ICGM, Univ. Montpellier, CNRS, ENSCM, F-34095 Montpellier, France

[6] CESAM and Physics of Solids, Interfaces and Nanostructures, B5, Université de Liège, B4000 Sart-Tilman, Belgium

[7] PGI 10 (Green IT), Forschungszentrum Jülich, 52428 Jülich, Germany

* These authors contributed equally

Table of content:

I. *Working hypothesis*

This work aims at answering the question, if metavalent bonding is a distinct, fundamental type of chemical bonding. It is critical, to verify or refute this hypothesis through carefully designed experiments. Such experiments are not only needed to further substantiate the claims of a novel, fundamental type of bonding. They are also important to understand the relationship between applications of chalcogenides and similar solids. If metavalent bonding is a fundamental bonding mechanism, distinctively different from covalent bonding, then one expects to find representative properties (e.g. Z*, ε_∞ and $\varepsilon(\omega)$), where the transition between metavalent and covalent bonding is characterized by significant, discontinuous property changes. If metavalent bonding is instead a variant of e.g. covalent bonding, we expect to find a rather continuous change for all relevant properties. In such a scenario, there would be no need to define a new class of materials (i.e. metavalent materials) with a distinctly different bonding mechanism. In case of a discontinuous change in relevant properties however, such a definition is justified and important. Studying the nature of the transition (i.e. its (dis-)continuity) from metavalent to covalent bonding in $GeTe_{1-x}Se_x$, $Sb_2Te_{3(1-x)}Se_{3x}$ and $Bi_{2-2x}Sb_{2x}Se_3$ allows to answer the question, whether or not metavalent bonding is a distinct, fundamental bonding type and if the definition of a new class of materials with a unique property portfolio (i.e. metavalent materials) is justified. Our working hypothesis is summarized in **Fig. S1** and in the following additional data for each pseudo-binary line are discussed.

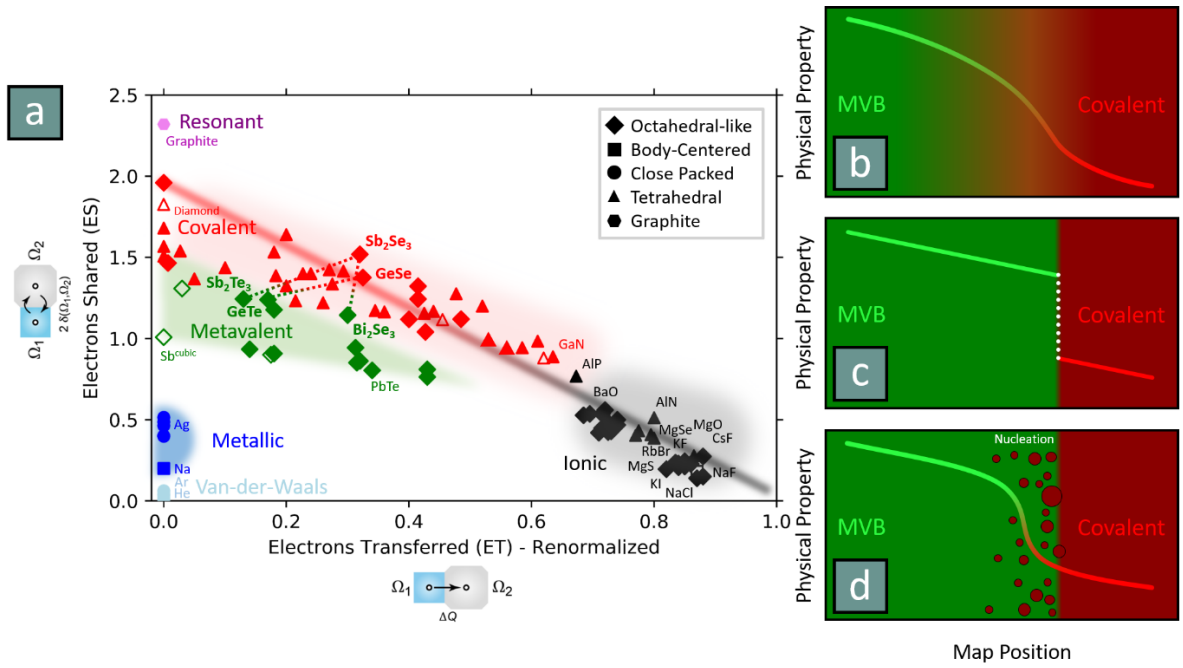

Fig. S1: Working hypothesis: In order to proof the hypothesis, that MVB is a distinct bonding type, the nature of the transition from metavalent to covalent bonding is studied for three different pseudo-binary lines: GeTe-GeSe, Sb_2Te_3-Sb_2Se_3 and from Bi_2Se_3-Sb_2Se_3 shown in a. Studying representative physical properties (e.g. Z*, ε_∞ and $\varepsilon(\omega)$) as a function of map position allows a distinction between a continuous (schematically shown in b) and discontinuous (schematically shown in c) change in physical properties. The latter then constitutes the distinct nature of metavalent bonding. If the phase transition is of first order, then the occurrence of nucleation and

growth as shown in d) is expected. In this case, it is important to ensure that the phase transformation between the phases is complete, as can be confirmed by XRD, for example. Please note, that b, c and d represent schematic drawings.

Interestingly, it is very difficult to find single phase compounds across the border from metavalent to covalent bonding even in isoelectronic solids. To illustrate the problem with some examples, several mono- and sesqui-chalcogenides are considered. While Sb_2Te_3 and Bi_2Te_3 (both show MVB) can be alloyed in any ratio and show no evidence for phase separation, upon alloying Sb_2Te_3 and Sb_2Se_3 (covalent bonding), phase coexistence of an orthorhombic Se rich phase (covalent) and a rhombohedral Te rich phase (MVB) is observed for a range of Se-Te mixtures. This is also observed for the mono-chalcogenides, where mixing MVB compounds such as PbSe and PbTe proceeds without phase separation, while alloying PbSe and SeSe (covalent) is accompanied by phase separation. It thus can almost be seen as serendipity that a single phase hexagonal GeTe-GeSe compound forms in the transition zone between rhombohedral (MVB) and orthorhombic (covalent) GeTe-GeSe compounds.

Interestingly, there is also no common ground in the crystal structures. The mono-chalcogenides with covalent bonding such as GeSe, SnSe, SnS or GeS possess an orthorhombic ground state, while the metavalent compounds have either a cubic or rhombohedral crystal structure. Hence, there is no group – subgroup relation between the different crystal structures across the covalent – MVB transition [1]. Such a phase transition cannot be continuous, i.e. second order but has to be a first order phase transition. First order phase transitions occur via nucleation and growth, as sketched in the revised figure S1. Hence, they can easily appear continuous in terms or their properties, since a mixture of two coexisting phases is studied. In this case it is crucial to ensure that the transformation between the two phases is complete if we want to compare the properties of the two phases.

The change in structure could be seen as the origin of the different properties, a concern we have already expressed in the manuscript. However, the discontinuous change of bond breaking observed in the atom probe as well as the ability to successfully classify the materials in groups according to their bonding and the discontinuous property change at the border clearly demonstrates that we observe a change of bonding.

II. <u>The pseudo-binary line $GeSe_xTe_{1-x}$:</u>

a. X-ray diffraction (XRD)

As shown in **Fig. S2**, XRD measurements of samples along the pseudo-binary line between GeTe and GeSe revealed three different crystallographic phases (rhombohedral (space group 160), hexagonal (space group 186) and orthorhombic (space group 62)). Starting from the metavalently bonded rhombohedral GeTe, the system remains rhombohedral up to a GeSe concentration of about 75%. For the entire stoichiometry range and all phases, a gradual shift of the XRD peak positions with increasing Se content is observed, which is due to the smaller size of the Se atom. The linear decrease of cell volume displayed in **Fig. S3** is strong evidence for the good miscibility of GeTe and GeSe, consistent with previous studies of bulk solid solutions.[2],[3] If films with a GeSe content between 50% and 75% are annealed for a longer time at elevated temperatures, a second, hexagonal crystalline phase is found.[4] The proportion of this hexagonal phase increases with increasing annealing time or increasing annealing temperature. At sufficiently long annealing or sufficiently high annealing temperature, a film can be produced which only contains the hexagonal phase, as verified by XRD (fig. S2) and Raman data (fig. S.5). Hence, it is possible to stabilize $GeSe_xTe_{1-x}$ films in this composition range in two different structures (without co-existence). Above 90% Se content, the covalently bonded, orthorhombic phase is obtained.

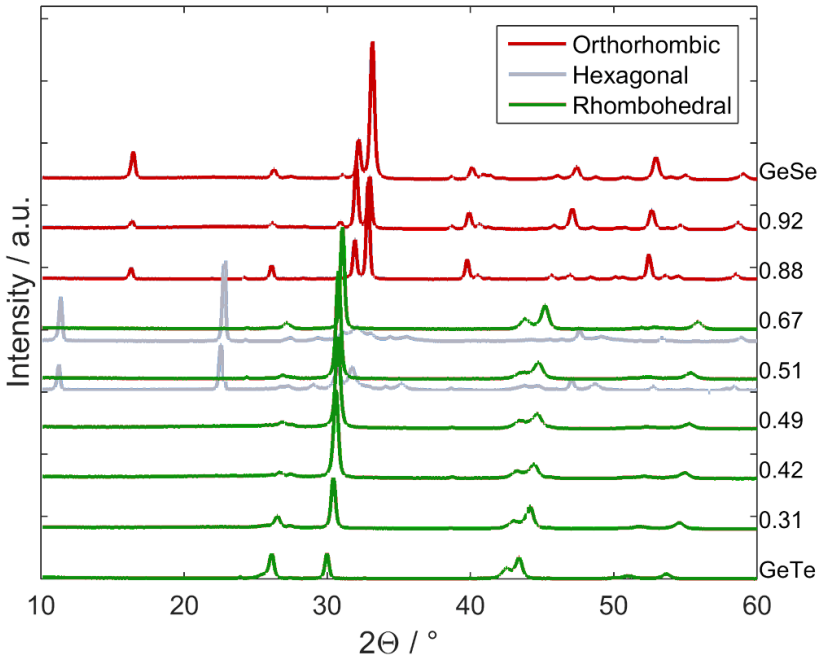

Fig. S2: XRD patterns of various $GeSe_xTe_{1-x}$ samples. Each pattern has been shifted by a constant y-offset**.** Three different crystalline phases are found for $GeSe_xTe_{1-x}$ alloys (rhombohedral, orthorhombic and hexagonal). All phases develop a characteristic pattern that shifts with stoichiometry. This is evidence for the formation of miscible solid solutions. All diffraction patterns can be indexed according to the corresponding space group, i.e. no secondary phases were observed. All films are polycrystalline.

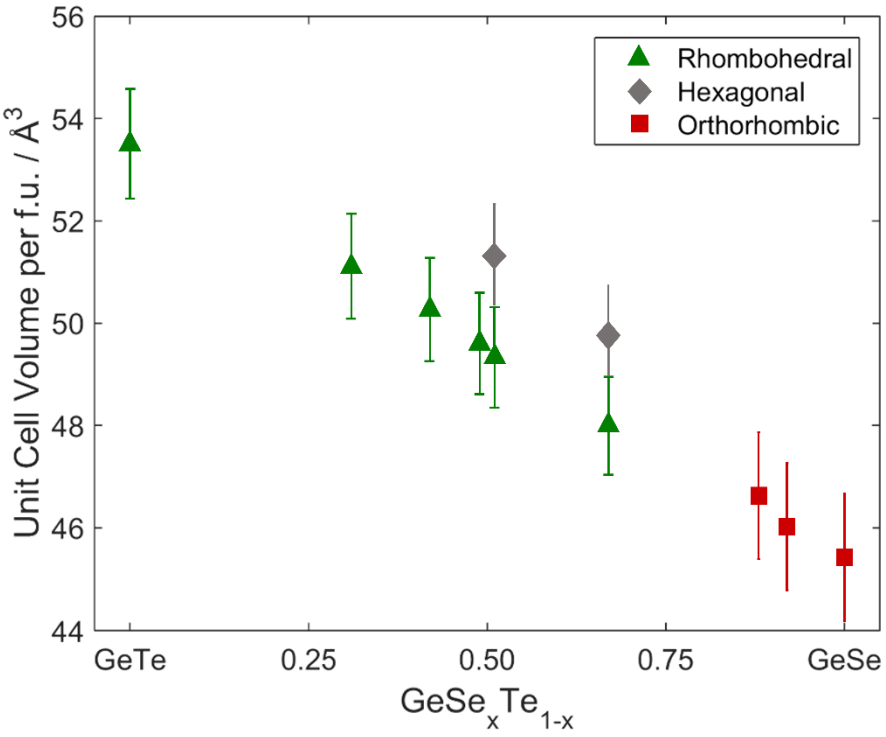

Fig. S3: Unit cell volume per formula unit of various compounds along the $GeSe_xTe_{1-x}$ pseudo-binary line. Three different crystalline phases are found for $GeSe_xTe_{1-x}$ alloys (rhombohedral, orthorhombic and hexagonal). For intermediate compositions on the pseudo-binary line, both a rhombohedral and a hexagonal phase can be formed, which also differ in unit cell volume and consequently in density. The unit cell volume of each crystalline phase varies linearly with composition (as predicted by Vegard's law). This implies that there is a good miscibility over the whole stoichiometry range.

b. X-ray reflectometry (XRR)

Fig. S4 shows experimental densities of the $GeSe_xTe_{1-x}$ films, obtained from XRR measurements. The density smoothly decreases as a function of stoichiometry. Hence, we can rule out a discontinuous change of the mass density due to the different atomic arrangement in rhombohedral and hexagonal/orthorhombic phases. We can therefore conclude, that the discontinuous change in ε_∞ discussed in the main text is not caused by a discontinuous change in mass density, but by a change in chemical bonding.

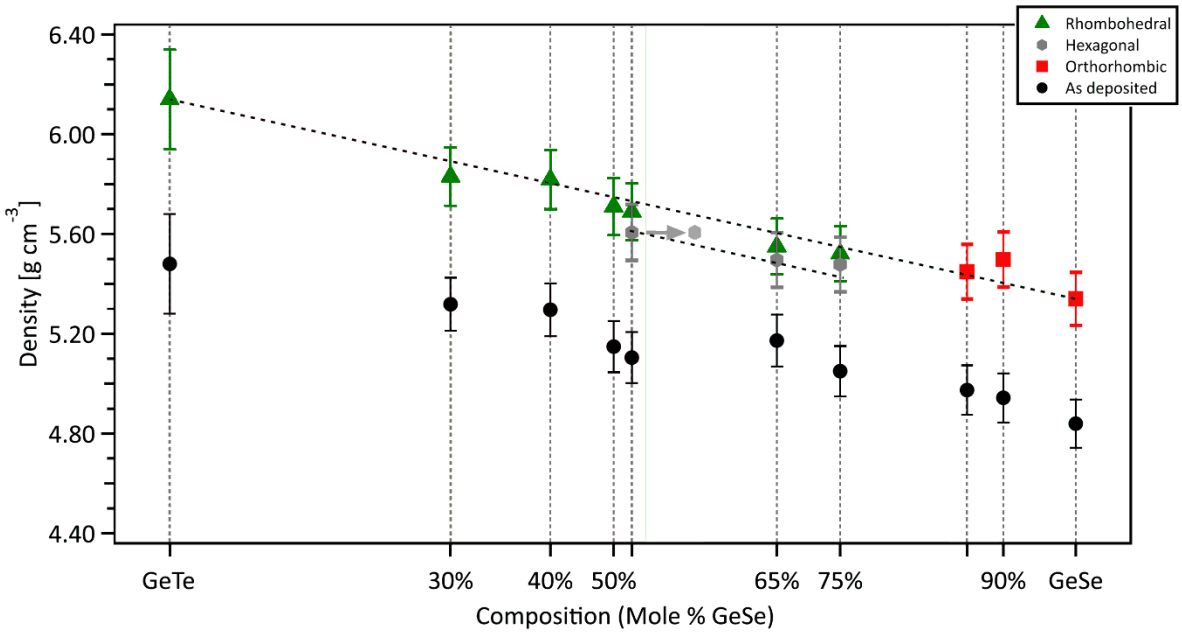

Fig. S4: Densities determined using X-Ray reflectometry (XRR). An overall decrease is observed with increasing GeSe content. This is due to the smaller mass of the Selenium atom as can be seen from **Fig. S3**.

c. Raman Spectroscopy

In order to explore the relationship between the change of bonding and atomic arrangement, i.e. the crystallographic structure, Raman measurements were performed. The corresponding results are depicted in **Fig. S5**. The three different crystalline phases (rhombohedral, hexagonal and orthorhombic) are characterized by rather different Raman spectra, indicative for significant differences in atomic arrangement. The Raman spectra of the rhombohedral phase show only faint, broad peaks characteristic for small deviations from a perfectly octahedral arrangement. In contrast, both the orthorhombic and hexagonal phases feature more Raman modes of higher intensity, suggestive of a pronounced deviation from a perfectly octahedral coordination.

This is depicted by the models for the octahedral-like rhombohedral phase (upper left inset of **Fig. S5**) and the more heavily distorted orthorhombic arrangement (lower right inset of **Fig. S5**). Hence there is a close correspondence between the three different types of XRD patterns and the three different types of Raman spectra. Moreover, a shift of the Raman modes with respect to stoichiometry is found confirming the miscibility of GeTe and GeSe.

We can therefore conclude, that the sudden drop in electronic polarizability shown in **Fig. 2** of the main text is also accompanied by the transition from the rhombohedral to the hexagonal phase with a concomitant change of the vibrational properties (as seen in the corresponding Raman spectra presented here). All spectra show characteristic modes of only one distinct crystallographic phase. For $GeSe_xTe_{1-x}$ films with a rhombohedral structure, only weak Raman modes are observed.

The low intensity for rhombohedral films is due to the octahedral-like atomic arrangement, as there are no Raman-active modes for a perfect octahedral arrangement.[5],[6] Distortions away from the perfect octahedral arrangement produce modes, which increase in intensity with increasing distortion. The transition to hexagonal $GeSe_xTe_{1-x}$ is accompanied by a significant intensity increase of the Raman modes, which also differ in frequency and number from those of the rhombohedral films. The orthorhombic phase is also characterized by relatively sharp and intense Raman peaks. The atomic arrangement hence differs significantly for the three crystallographic phases.

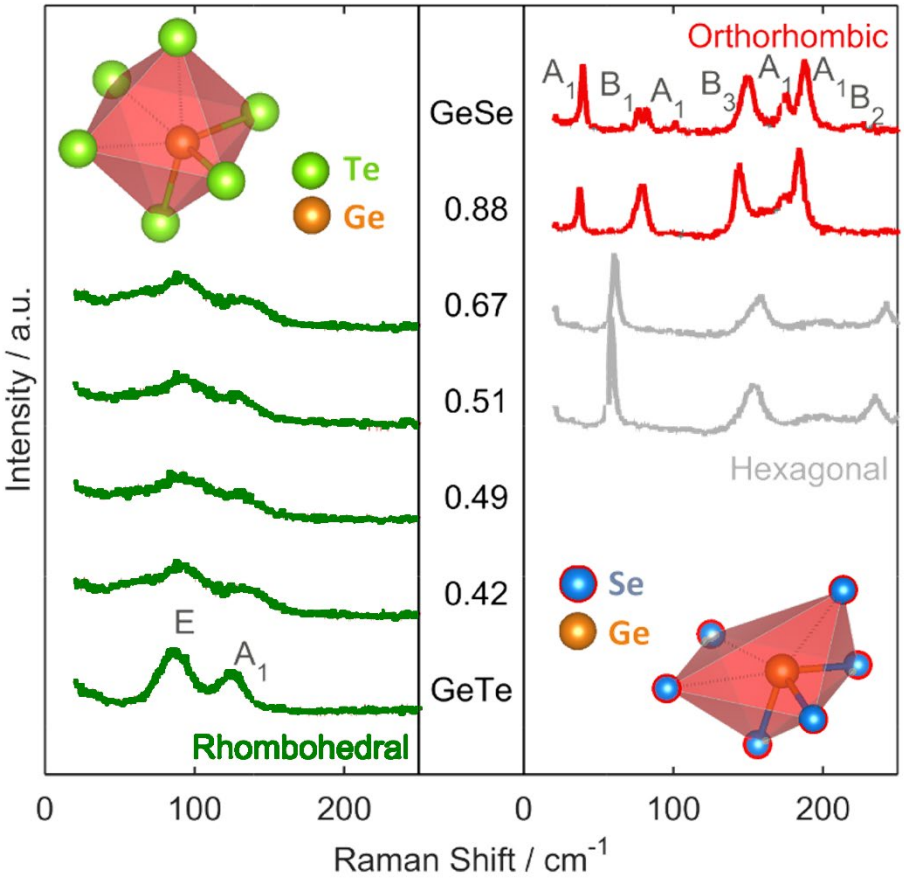

Fig. S5: Raman spectra of various stoichiometries along the pseudo-binary line between GeTe and GeSe. All spectra are shifted by a vertical offset**.** The stoichiometry of the samples is listed in the middle column next to the corresponding spectra.

III. *The pseudo-binary line $Sb_2Te_{3(1-x)}Se_{3x}$:*

a. *X-ray diffraction (XRD)*

In the following the comprehensive changes of XRD patterns and Raman spectra upon alloying Sb_2Te_3 with Sb_2Se_3 are discussed. **Fig. S6** shows the XRD patterns of the $Sb_2Se_{3x}Te_{3(1-x)}$ samples studied here. Up to a Se content of 60%, rhombohedral (space group 160) films are formed, while orthorhombic (space group 62) films are found for a Se content above 70%, as evidenced by an accompanying change of the XRD patterns. For the entire stoichiometry range and all phases, a gradual shift of the XRD peak positions with increasing Se content is observed, which is due to the smaller size of the Se atom. The linear decrease of cell volume displayed in **Fig. S7** is strong evidence for the good miscibility as it was also observed for the $GeSe_xTe_{1-x}$ pseudo-binary line.

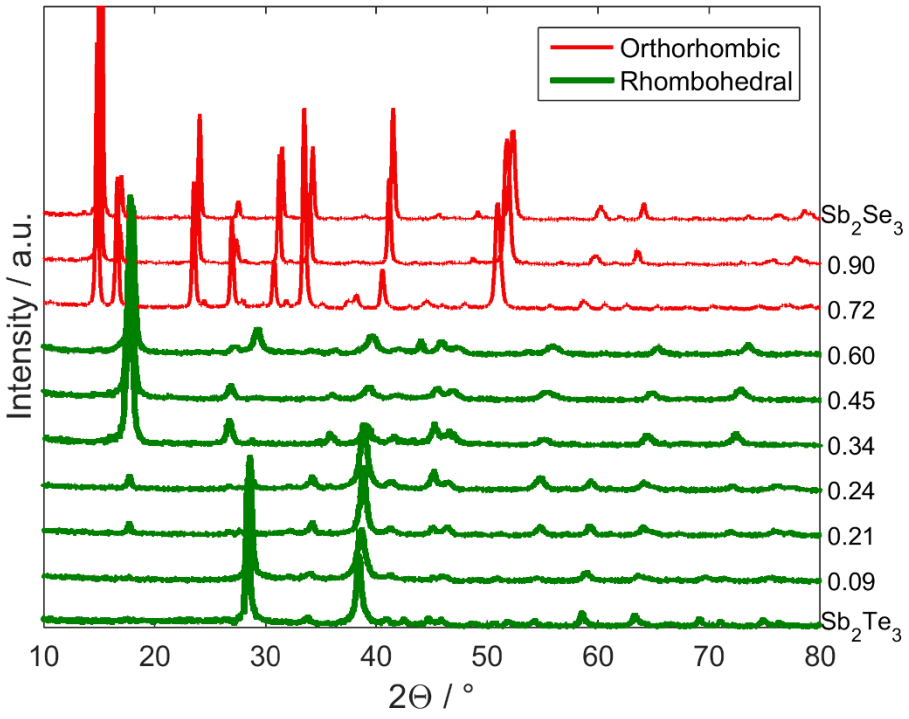

Fig. S6: XRD patterns of $Sb_2Se_{3x}Te_{3(1-x)}$ samples. Each XRD pattern has been shifted by a constant y-offset**.** Two different crystallographic phases can be identified along the $Sb_2Se_{3x}Te_{3(1-x)}$ line, which is the rhombohedral Sb_2Te_3 phase and the orthorhombic Sb_2Se_3 phase. A monotonous peak shift of the patterns is observed upon alloying which is evidence for the miscibility of the materials. Moreover, no investigated compound features a superposition of both the rhombohedral and orthorhombic pattern ruling out phase coexistence. Although some intensity changes are observed in the rhombohedral phase, the presence of several peak families in every pattern provides evidence for the polycrystalline nature of the films.

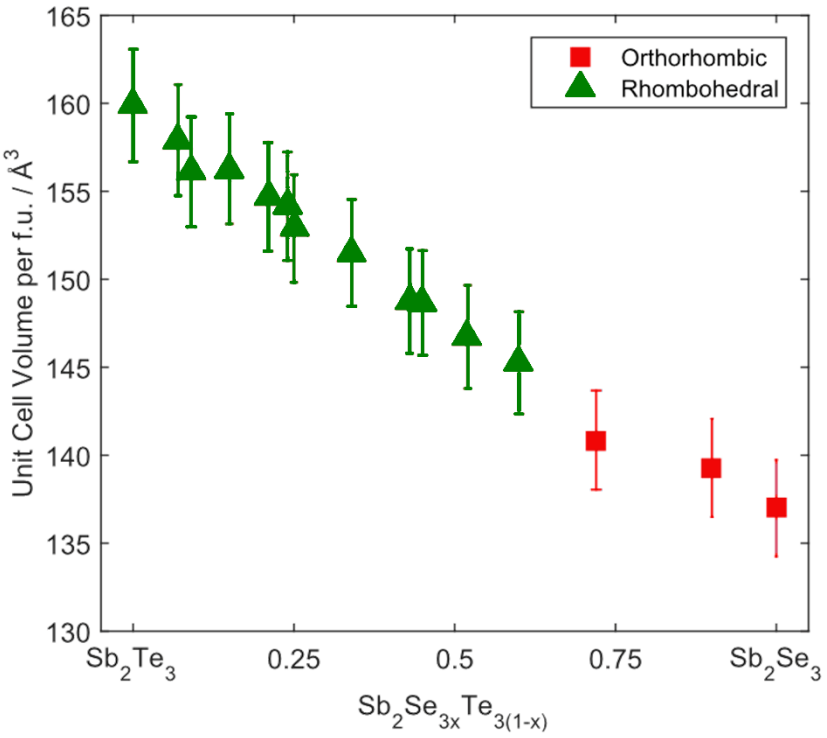

Fig. S7: Unit cell volume per formula units of various compounds along the pseudo-binary line $Sb_2Se_{3x}Te_{3(1-x)}$. Two different crystalline phases are found (rhombohedral and orthorhombic). The unit cell volume of each crystalline phase varies linearly with composition (as predicted by Vegard's law). This is evidence for the good miscibility of Sb_2Te_3 and Sb_2Se_3.

b. X-ray reflectometry (XRR)

Fig. S8 shows experimental densities of the $Sb_2Se_{3x}Te_{3(1-x)}$ films, obtained from XRR measurements. Also within this pseudo-binary line, no discontinuous changes of the mass density due to the different atomic arrangement in the rhombohedral and orthorhombic phases are observed. As in the case of the $GeSe_xTe_{1-x}$ pseudo-binary line, we can conclude, that the discontinuous change in ε_∞ discussed in the main text is not caused by a discontinuous change in mass density, but rather by changes in chemical bonding. These findings suggest, that this discontinuity of the electronic polarizability between metavalent and covalent bonding in the $GeSe_xTe_{1-x}$ system is a rather generic feature.

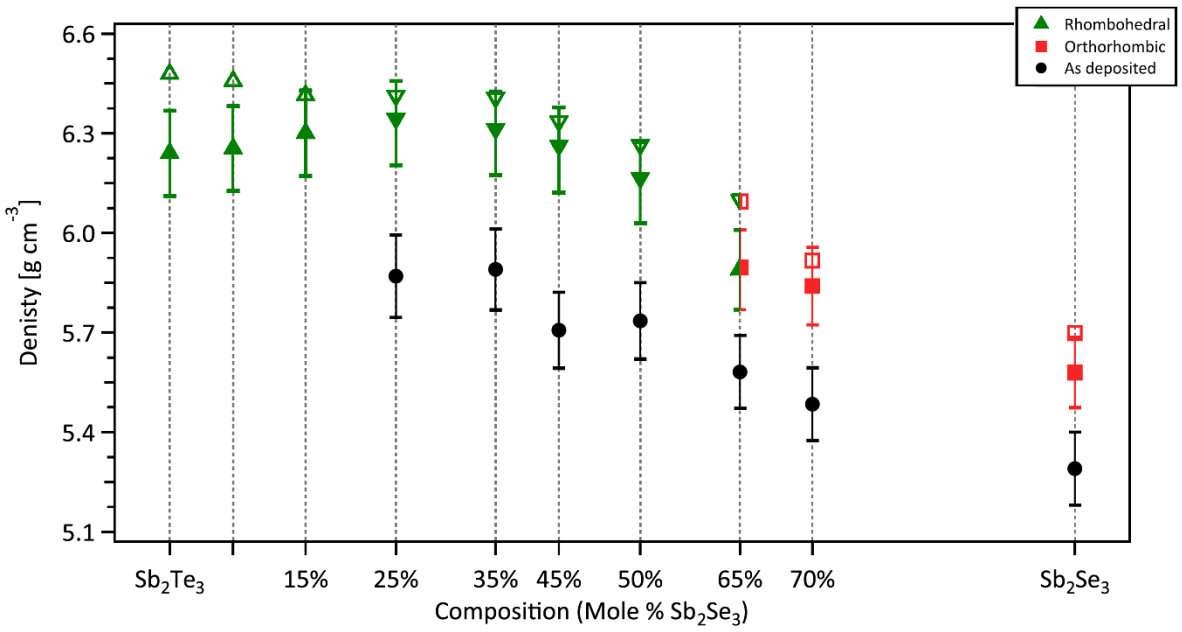

Fig. S8: Densities determined using X-Ray reflectometry (XRR). An overall decrease is observed with increasing Sb_2Se_3 content. This is due to the smaller unit cell volume as can be seen from **Fig. S7**.

c. Raman Spectroscopy

Also in the case of the $Sb_2Se_{3x}Te_{3(1-x)}$ pseudo-binary line, Raman measurements were performed in order to investigate the relationship between the change of bonding and atomic arrangement, i.e. the crystallographic structure. The corresponding Raman spectra and modes are depicted in **Fig. S9**. Down to 7 % Sb_2Se_3 the rhombohedral phase shows, similar to the $GeSe_xTe_{1-x}$ line, only faint, broad peaks due to the small deviations from a perfectly octahedral coordination. Below this Sb_2Se_3 content, the Raman peaks are sharpening slightly due to an increased deviation from a perfect O_h symmetry. The highest energy mode of Sb_2Te_3 (169 cm^{-1}) shows a pronounced shift to higher energies. This behavior can be explained by the initial incorporation of Se on the Te2 site follow by a random incorporation of Se on the Te1 site above a Sb_2Te_3 concentration of 33%. Differences in the Raman spectra between the rhombohedral and the orthorhombic phases are also clearly visible. Hence, the atomic arrangement and vibrational properties differ significantly between these two crystallographic phases as anticipated from the XRD analyses.

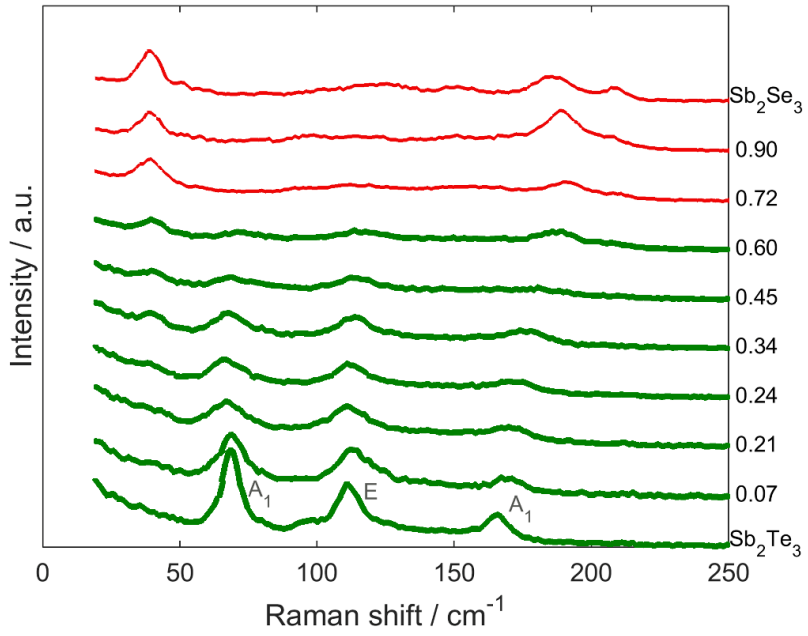

Fig. S9: Raman spectra of various $Sb_2Se_{3x}Te_{3(1-x)}$ samples. Each spectrum has been shifted by a constant y-offset**.** The modes of the rhombohedral Sb_2Te_3-phase can be identified. The orthorhombic compounds show different vibrational modes.

d. *Optical properties*

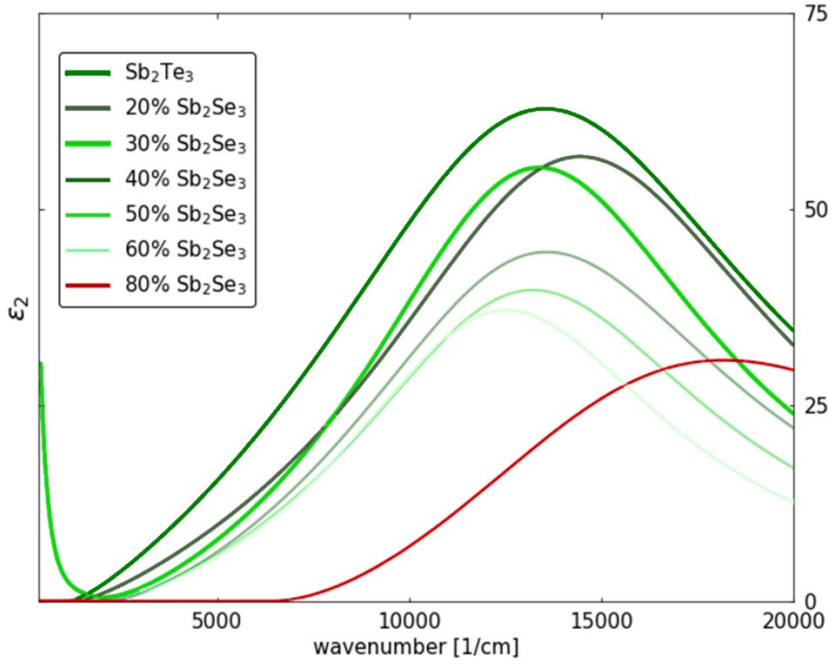

Fig. S10: Imaginary part of the dielectric function of $Sb_2Se_{3x}Te_{3(1-x)}$ compounds: There is a distinct jump in the dielectric function upon transition from metavalent (up to 60% Sb_2Se_3) to covalent bonding (at and above 80% Sb_2Se_3). The large maximum value of $\varepsilon_2(\omega)$ has been attributed to the alignment of the p-orbitals of adjacent atoms.[7] Its decrease observed for the materials studied here is hence indicative for a reduction of this alignment, i.e. an increased Peierls distortion. The sudden change of the size of the $\varepsilon_2(\omega)$ maximum is thus indicative for a discontinuous change of this alignment upon increasing Se content.

IV. *The pseudo-binary line $Bi_{2-2x}Sb_{2x}Se_3$*

a. *X-ray diffraction (XRD)*

XRD measurements were performed on eleven crystalline $Bi_{2-2x}Sb_{2x}Se_3$ samples of various stoichiometries (*cf.* **Fig. S11**). From 0% to 40% Bi_2Se_3 content (red), the samples are orthorhombic (space group 62), while for 90% and 100% (green) Bi_2Se_3 content they are rhombohedral (space group 160). Samples in the range between 50% and 80% Bi_2Se_3 content (purple) belong to the two-phase region of the phase diagram containing an orthorhombic and a rhombohedral phase. The evolution of the unit cell volume as a function of composition is shown in **Fig. S12**. The unit cell volume of the orthorhombic phase varies linearly with composition (as predicted by Vegard's law). Due to the difficulty to obtain crystalline samples of high quality on the Bi_2Se_3-rich side of the phase diagram, only 2 samples with sufficient quality could be obtained and used for our study. Hence, no conclusion concerning the cell volume evolution as a function of composition could be made. The miscibility gap in the Bi_2Se_3 – Sb_2Se_3 phase diagram makes it more difficult to follow the collapse of MVB in this system compared to the other two pseudo-binary lines. However, we will demonstrate in the following, that it is still possible.

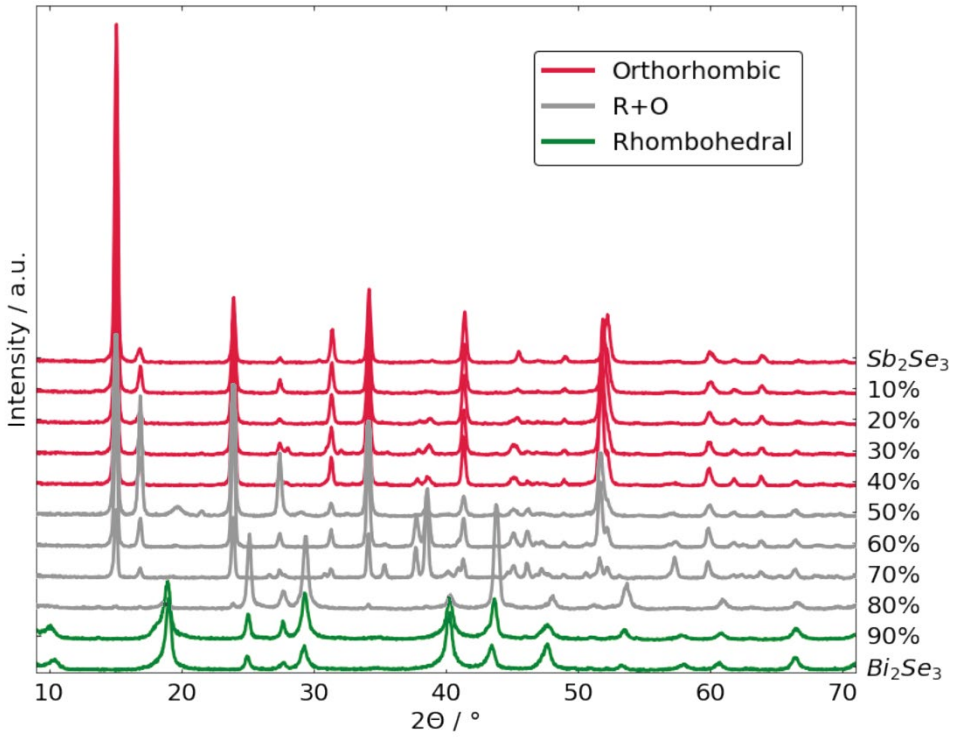

Fig. S11: XRD patterns of $Bi_{2-2x}Sb_{2x}Se_3$ samples. An orthorhombic (space group 62), a rhombohedral (space group 160) and a two-phase region are observed, confirming the Bi_2Se_3 – Sb_2Se_3 phase diagram.

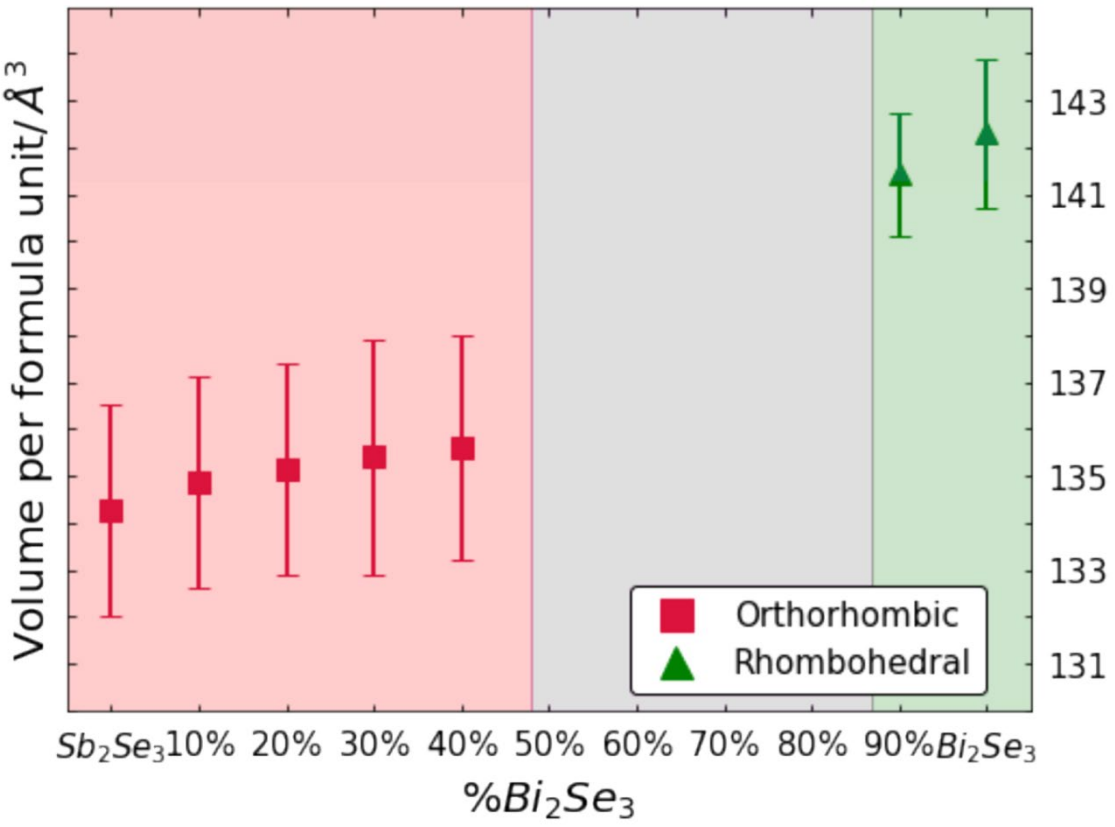

Fig. S12: Unit cell volume per formula units of various $Bi_{2-2x}Sb_{2x}Se_3$ samples. Two different crystalline phases (rhombohedral and orthorhombic) as well as a two-phase region was found. Hence, the unit cell volume could only be determined in the single-phase region. Our findings confirm the miscibility gap in the Bi_2Se_3 – Sb_2Se_3 phase diagram.

b. Optical properties

In order to study the collapse of MVB in the $Bi_{2-2x}Sb_{2x}Se_3$ system, we follow the evolution of the optical dielectric constant ε_∞ as a function of composition. The corresponding results are shown in **Fig. S13**. Please note, that values of ε_∞ within the miscibility gap are provided for the sake of completeness and have to be treated with care. However, the obtained values compare reasonably well with those found for the single-phase regions and they provide further insight in the nature of the bonding transition in the sense, that it already has its onset within the Bi_2Se_3-dominant side of the two-phase region, where ε_∞ increases by 26 %. The overall increase in ε_∞ going from purely covalent to fully metavalent is 46 %. This example demonstrates, that it is possible to follow the transition, it is however recommended to choose systems without a miscibility gap to study such kind of bonding transitions in order to avoid a compositional broadening of the transition. However, in this case it provided valuable insight since we were able to compare the transition in systems with and without miscibility gap and we could confirm, that MVB collapses regardless, whether elemental substitutions are made on the anion or cation position of such kind of binary systems.

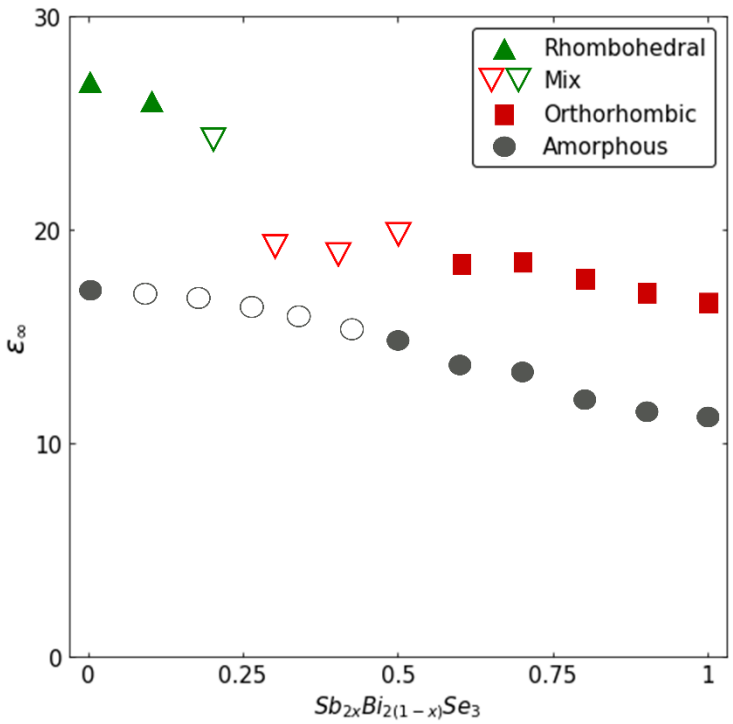

Fig. S13: Optical dielectric constant (ε_∞) along the $Bi_{2-2x}Sb_{2x}Se_3$ pseudo-binary line. As soon as the rhombohedral structure dominates a discontinuous increase of ε_∞ is observed, which is indicative for a transition from MVB to covalent bonding similar to those observed in the other two pseudo-binary systems. The difference here is a compositional broadening of the transition due to the miscibility gap, where values of ε_∞ must be interpreted with care.

c. X-ray reflectometry (XRR)

Fig. S14 shows the experimental densities of the $Bi_{2-2x}Sb_{2x}Se_3$ films obtained from XRR measurements. Also within this pseudo-binary line, no discontinuous change of the mass density due to the different atomic arrangement in the rhombohedral and orthorhombic phases is observed. However, it is noteworthy, that at the onset of the bonding transition within the two-phase region, the mass density is slightly lower (*cf.* **Fig. S14**), i.e. ε_∞ is probably slightly underestimated at this composition. As in the case of the $GeSe_xTe_{1-x}$ system, we can conclude, that the discontinuous change in ε_∞ discussed before is not caused by a discontinuous change in mass density, but rather by changes in chemical bonding.

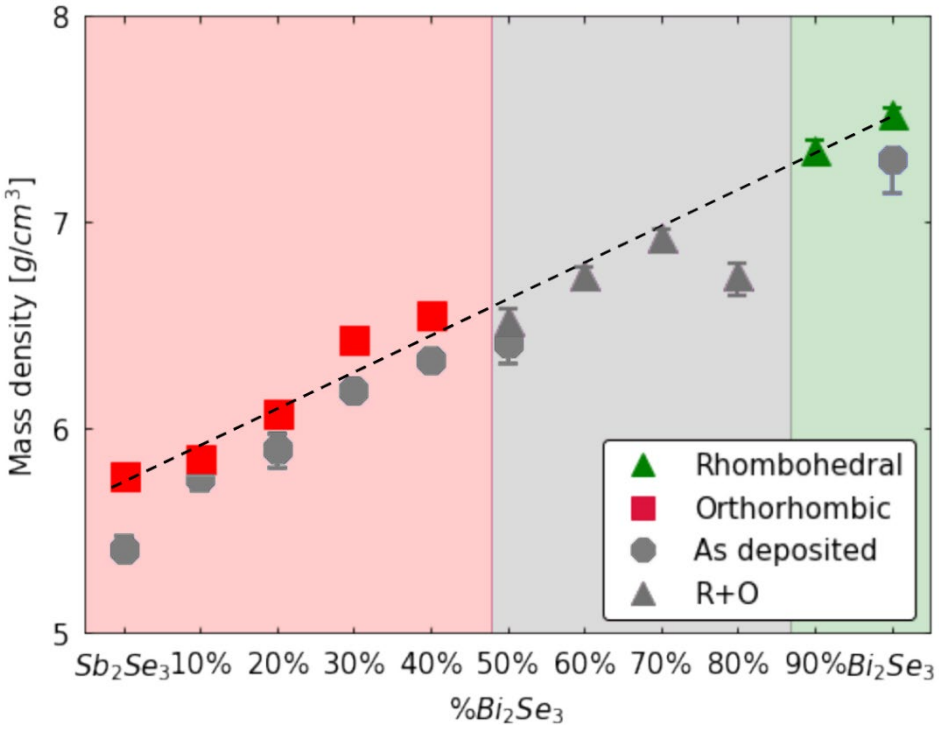

Fig. S14: Mass density of the $Bi_{2-2x}Sb_{2x}Se_3$ samples obtained from XRR measurements. As deposited (blue) and crystalline phases (red, purple and green) are plotted. An almost continuous increase is observed. At the onset of the bonding transition within the two-phase region, the mass density slightly decreases, i.e. ε_∞ (*cf.* **Fig. S11**) is probably slightly underestimated at this composition.

d. Raman spectroscopy

Also in the case of the $Bi_{2-2x}Sb_{2x}Se_3$ pseudo-binary line, Raman measurements were performed in order to investigate the relationship between the change of bonding and atomic arrangement, i.e. the crystallographic structure. The corresponding Raman spectra and modes are depicted in **Fig. S15 and Fig. S16**. The three modes of Sb_2Se_3 can be distinguished.

1. The E^2_g mode, which corresponds to the vibration of the Se-Se bonds and which is present up to 70%.
2. The A^2_{2u} mode corresponding to the vibration of the Sb-Sb bonds. This mode is visible up to 10%.
3. The A^2_{1g} mode corresponding to the vibration of the Sb-Se bonds. Like the E^2_g mode, this mode persists up to 30% with a pronounced red shift when moving towards Bi_2Se_3.

While the Se-Se mode is essentially invariant up to 70%, the Sb-Sb and Sb-Se bond vibrations are significantly changing. This seems coherent with the expectation that, along this pseudo-binary line, major changes occur on the cation sub-lattice, which also results in a bonding transition from MVB to covalent bonding.

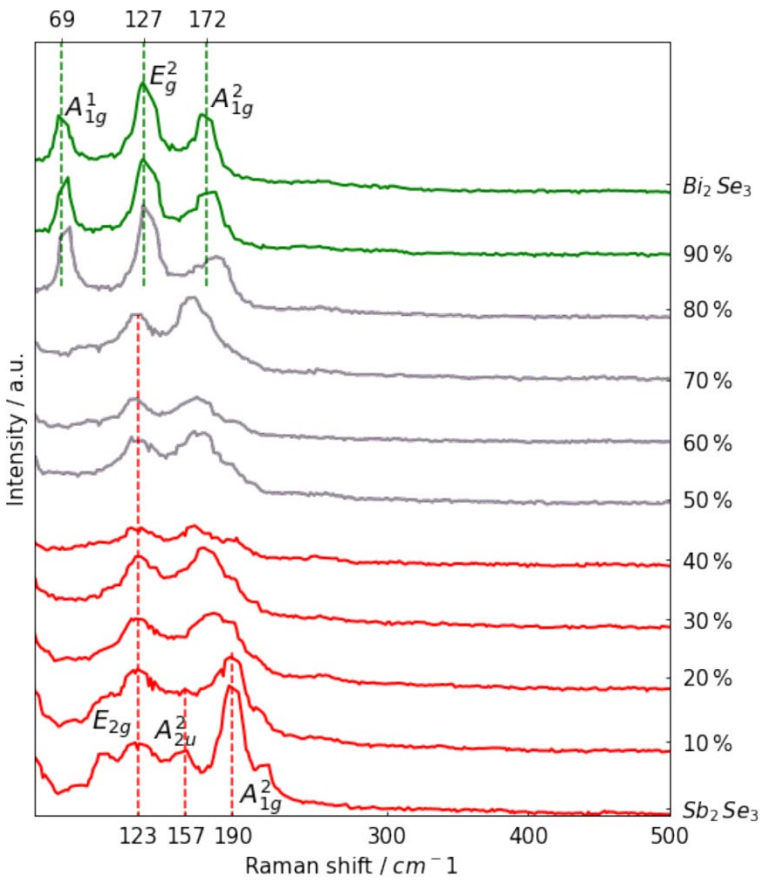

Fig. S15 Raman spectra of various $Bi_{2-2x}Sb_{2x}Se_3$ samples.

Sb_2Se_3			Bi_2Se_3		
Mode	Stokes shift	Vibration	Mode	Stokes shift	Vibration
E_{2g}	$\sim 123\,cm^{-1}$	$Se-Se$ bonds	A_{1g}^1	$\sim 69\,cm^{-1}$	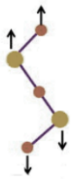
A_{2u}^2	$\sim 157\,cm^{-1}$	$Sb-Sb$ bonds	E_g^2	$\sim 127\,cm^{-1}$	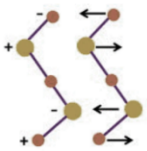
A_{1g}^2	$\sim 190\,cm^{-1}$	$Sb-Se$ stretching $SbSe_{3/2}$ pyramids	A_{1g}^2	$\sim 172\,cm^{-1}$	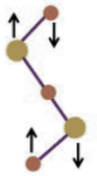

Fig. S16 Corresponding Raman modes of Bi_2Se_3 and Sb_2Se_3.

V. *Atom Probe Tomography and the Probability of Multiple Events*

To confirm that the discontinuous property changes described above and in the main text are indeed due to changes in bonding, systematic studies of bond breaking were performed. It has recently been shown, that atom probe tomography (APT) and specifically the probability of detecting multiple events (PME) by the detector of the atom probe distinguishes the different bond breaking behavior.[8] It is noteworthy, that such an analysis is independent of the corresponding crystal structure of the compound of interest. The corresponding probabilities of multiple events (PMEs) of all the end members of the three systems studied here are summarized in **Fig. S17.** On every pseudo-binary line, a PME drop occurs when going from the corresponding metavalent (i.e. Sb_2Te_3, GeTe and Bi_2Se_3) to the covalent end members (i.e. GeSe, Sb_2Se_3).[8-9] Hence, there has to be a change in chemical bonding somewhere along each pseudo-binary line. Recently, this transition was explored in more detail for the $GeTe_{1-x}Se_x$ pseudo-binary line (*cf.* **Fig. S18**).[8] These experiments show a transition from metavalent to covalent bonding between x = 0.5 and x = 0.75, which is consistent with the data presented in the main manuscript. Since probing the probability of multiple events is independent of the crystal structure, we can conclude that the changes, we observe in the optical properties are inherently connected to a change in chemical bonding.

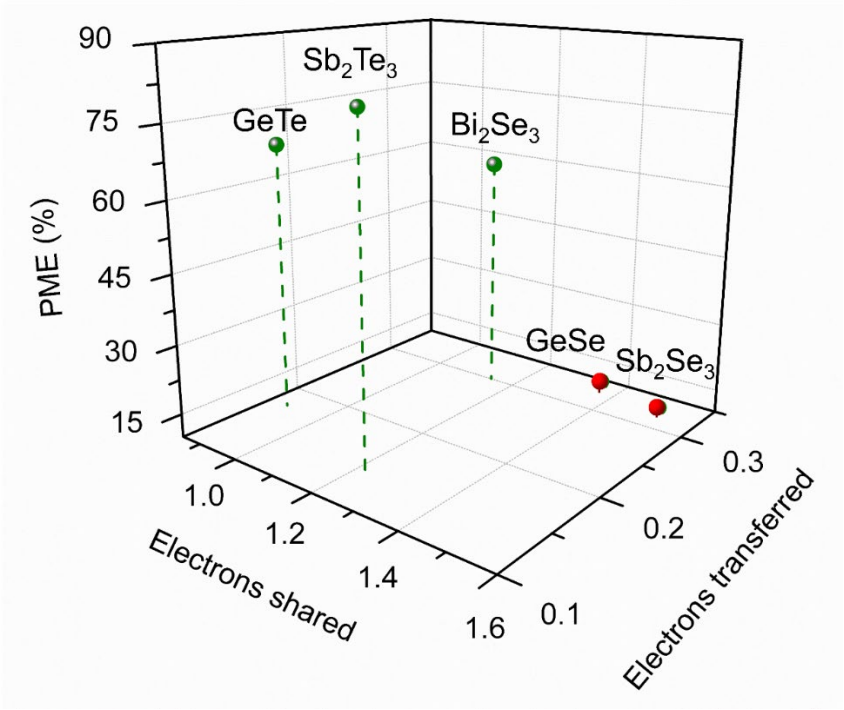

Fig. S17: Probability of multiple events (PME) correlated with the electrons shared and transferred between adjacent atoms. This figure shows the end-members of the corresponding pseudo-binary lines. The difference in PME values between the metavalently and covalently bonded end-members of each pseudo-binary line suggests, that one can expect a transition between these two bonding mechanisms along each pseudo-binary line, which we demonstrated in this manuscript.

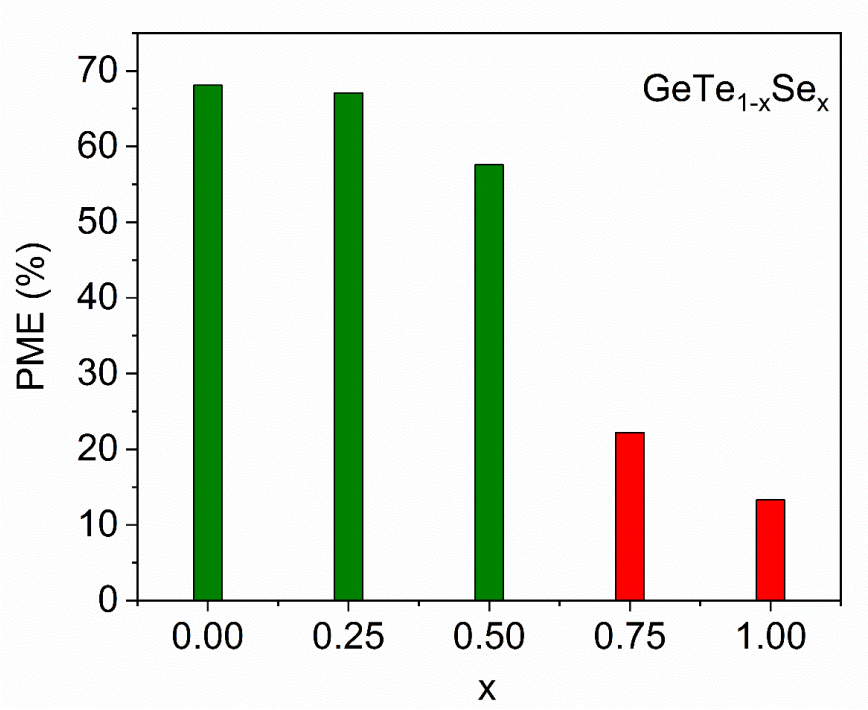

Fig. S18: Probability of multiple events (PME) along the $GeTeSe_x$ pseudo-binary line: Atom Probe Tomography experiments confirm the transition from metavalent to covalent bonding between x = 0.5 and x = 0.75, which is consistent with the data presented in the main manuscript. Since probing the probability of multiple events is independent of the crystal structure, we can conclude that the changes, we observe in the optical properties are inherently connected to a change in chemical bonding. The PME values were extracted from Ref. [8].

VI. Linking optical properties with chemical bonding

In the main manuscript we show and discuss systematic changes in the optical absorption, i.e. $\varepsilon_2(\omega)$, in the $GeTe_{1-x}Se_x$ series upon experimentally changing the composition and upon theoretically changing the degree of the Peierls distortion (i.e. the R_{long}/R_{short} ratio) in GeTe. Here, we provide a theoretical framework, which describes the link between $\varepsilon_2(\omega)$ and orbital overlap, i.e. chemical bonding. Semiconductors and insulators possess a fundamental absorption edge in the NIR, VIS or UV range, depending on the solid and its band structure. This absorption edge is a result of optical excitations from the onset of the optical transitions across the fundamental band gap.

Optical interband transition from an initial to a final state can be described energetically as follows:

$$E_f = E_i + \hbar\omega \qquad (1)$$

E_i: initial state energy, E_f: final state energy, $\hbar\omega$: energy of the absorbed photon

Indeed, in chemistry, the quantum mechanical transition rate for direct optical interband absorption is given by:

$$W_{i\to f} = \frac{2\pi}{\hbar}|M|^2 g(\hbar\omega)$$

(2)

i: initial state, f: final state, M: matrix element, g ($\hbar\omega$): joint density of states, $\hbar$: reduced Planck constant

Hence, optical absorption depends on the joint density of states and the matrix element (M) from which optical interband transition rules can be obtained.

Switching to the solid state case, and using the Random Phase Approximation (RPA) the imaginary part of the dielectric function can be written as:

$$\varepsilon^{(2)}_{\alpha\beta}(\omega) = \frac{4\pi^2 e^2}{\Omega} lim_{q\to 0} \frac{1}{q^2} \sum_{c,v,\boldsymbol{k}} 2\,\omega_{\boldsymbol{k}} \delta(\varepsilon_{c\boldsymbol{k}} - \varepsilon_{c\boldsymbol{k}} - \omega) \times \langle u_{c\boldsymbol{k}+\boldsymbol{e}_\alpha q} | u_{v\boldsymbol{k}} \rangle \left\langle u_{v\boldsymbol{k}} \middle| u_{c\boldsymbol{k}+\boldsymbol{e}_\beta q} \right\rangle \qquad (3)$$

With c and v designing the valence and conduction states, u_{ck} describing the cell periodic part of the orbital at the k-point $\mathbf{k}$ and $\mathbf{e}_\alpha$ denoting the unit vectors in the three Cartesian directions.[10] This expression allows to identify two features. First the Kronecker function corresponds to a joint density of states, and the last product consists of overlap integrals. By comparing expressions (2) and (3), one can thus understand how, in the solid, the absorption at a given energy depends on both the joint density of states and the orbital overlap.

This is clearly visible in our data shown in the main manuscript since orbital overlap can be influenced by the degree of Peierls distortion (i.e. the R_{long}/R_{short} ratio) and electron transfer[11], which has clear effects on the matrix element[11] and in turn on $\varepsilon_2(\omega)$. Optical absorption, i.e. $\varepsilon_2(\omega)$, therefore provides significant insights into chemical bonding in solids. This link between chemical bonding and optical properties also provides the opportunity to tailor opto-electronic properties of solids by means of chemical bonding considerations (e.g. by using ES and ET as the natural variables of chemical bonding in solids) as demonstrated in the main text and in Ref. [11].

VII. *Elipsometry fits*

The imaginary part of the dielectric functions shown in Fig. 5 of the main manuscript were obtained from fitting experimental elipsometry data. **Fig. S19** and **Fig. S20** summarize these fits.

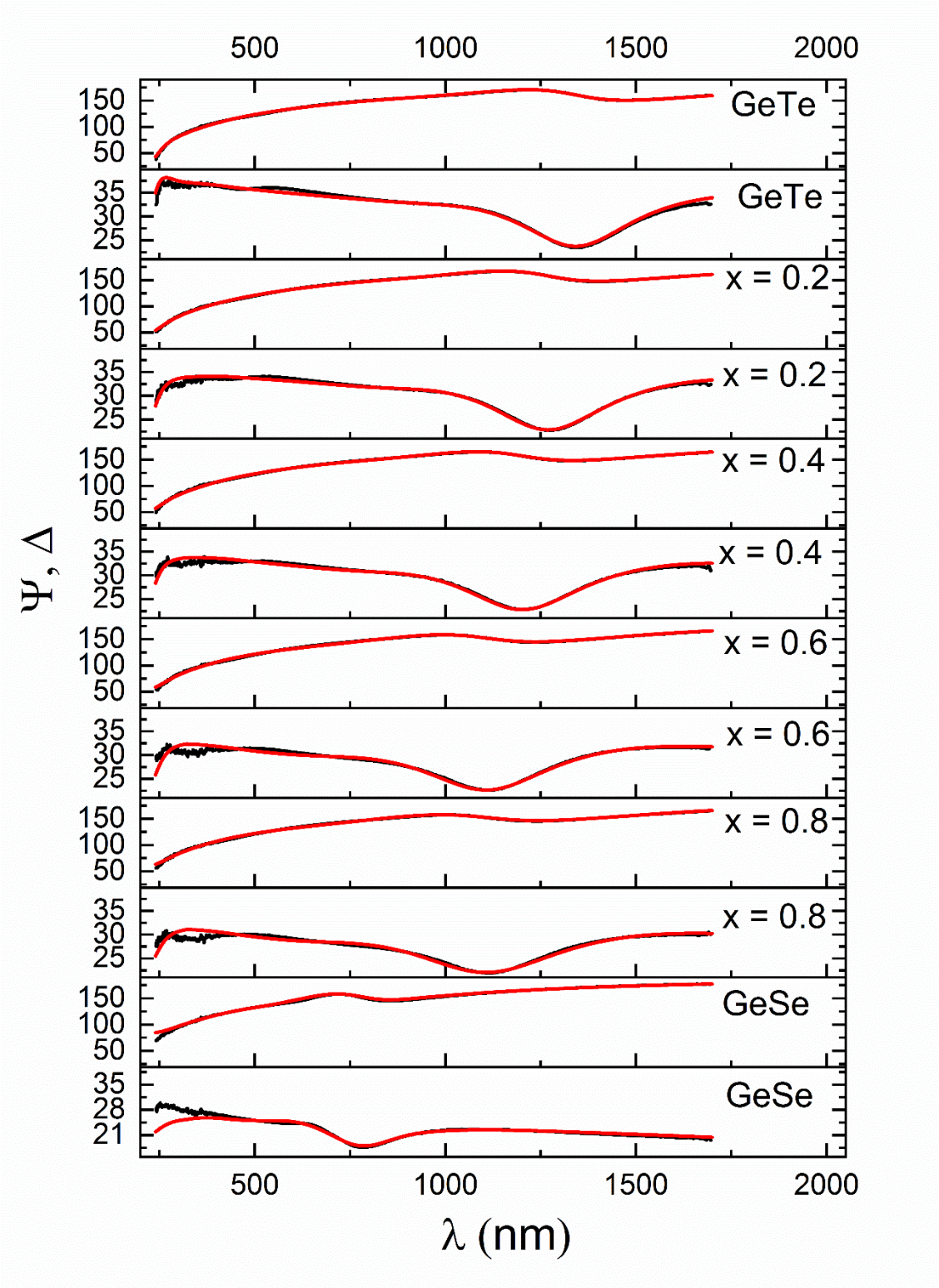

Fig. S19: Elipsometry fits (red) of crystalline $GeTe_{1-x}Se_x$ data (black): The corresponding imaginary parts of the dielectric functions can be found in Fig. 5 of the main manuscript.

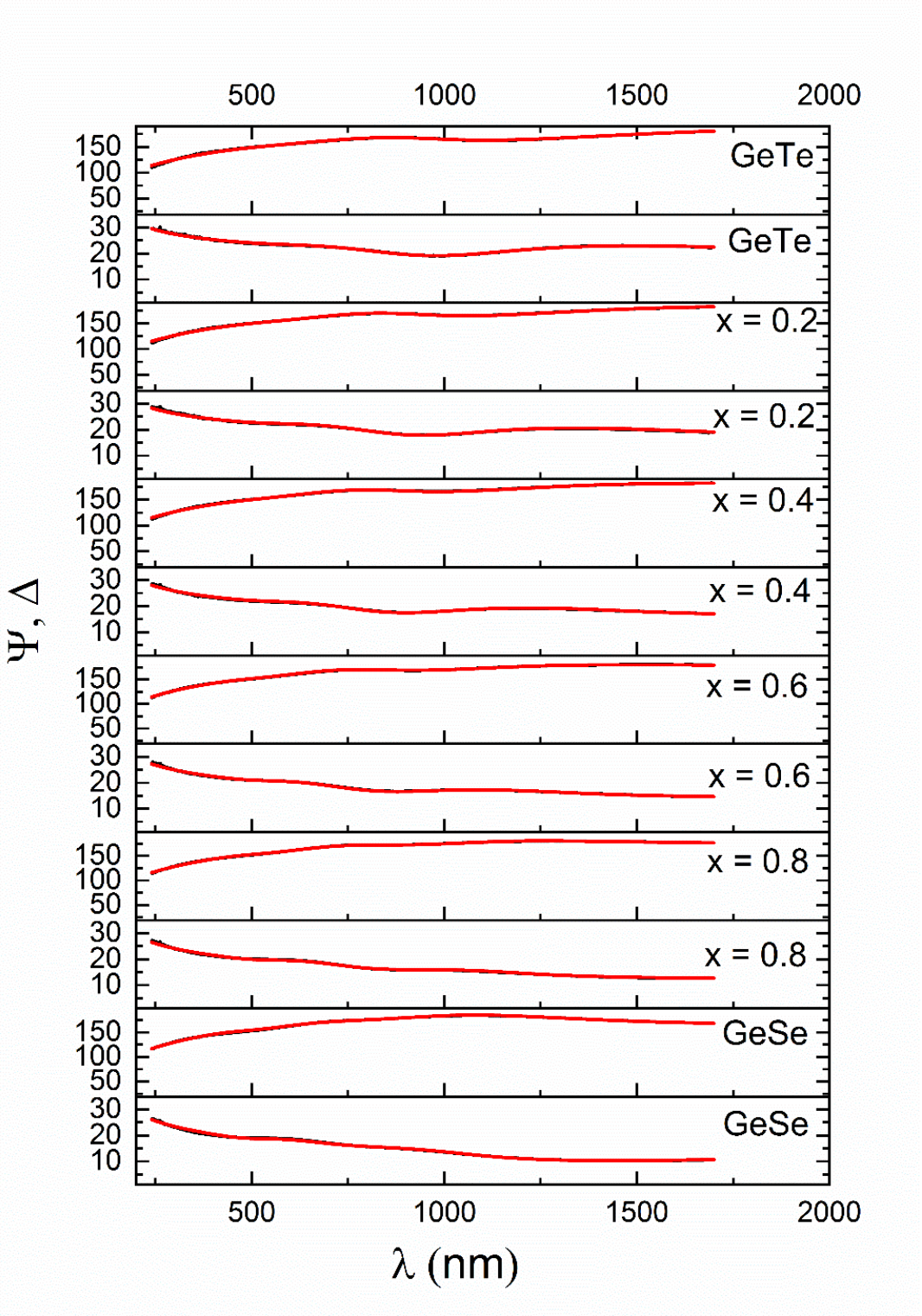

Fig. S20: Elipsometry fits (red) of amorphous $GeTe_{1-x}Se_x$ data (black): The corresponding imaginary parts of the dielectric functions can be found in Fig. 5 of the main manuscript.

VIII. Technical details

a. The Clausius-Mossotti relation

The Clausius-Mossotti equation connects the macroscopic permittivity ϵ with the microscopic polarizabilities α. It can be written as[12]

$$\frac{\epsilon-1}{\epsilon+2} = \frac{\rho}{3\epsilon_0}\frac{\sum n_i\alpha_i}{\sum n_i m_i} \quad , \tag{10}$$

where ρ denotes the mass density, ϵ_0 is the vacuum permittivity and $\sum n_i\alpha_i$, $\sum n_i m_i$ are the average (electronic) polarizability and atomic mass, respectively. By setting $\epsilon = \epsilon_\infty$ we associate the corresponding α_i with electronic or bond polarizabilities of the respective atom. To extract the bond polarizabilities, we set up a system of non-linear equations of the form

$$S = \begin{cases} \frac{\epsilon_{\infty,1}-1}{\epsilon_{\infty,1}+2} = \frac{\rho_1}{3\epsilon_0}\frac{\sum n_{1,i}\alpha_i}{\sum n_{1,i}m_i} \\ \cdot \\ \cdot \\ \cdot \\ \frac{\epsilon_{\infty,j}-1}{\epsilon_{\infty,j}+2} = \frac{\rho_j}{3\epsilon_0}\frac{\sum n_{j,i}\alpha_i}{\sum n_{j,i}m_i} \end{cases} , \tag{11}$$

where *j* is the number of compounds. A non-linear least squares algorithm is utilized to obtain a set of polarizabilities α_i which satisfy the equation system. The results of the refinements are shown and discussed in the main text.

b. Extracting the Born effective charge

In the harmonic approximation, the dielectric susceptibility (χ) of a polar (IR active) phonon is a Lorentz oscillator:[13]

$$\chi(\omega) = \frac{\Delta\epsilon\Omega_0^2}{\Omega_0^2-\omega^2-i\gamma\omega} \quad , \tag{12}$$

where Ω_0 is the phonon resonance frequency, γ its inverse lifetime (or damping) and $\Delta\epsilon$ its contribution to the dielectric constant. The numerator of equation (12) is also called the phonon plasma frequency. It is a measurement of the transverse effective charge (q_T) involved in the vibration:

$$\Omega_p^2 = \Delta\epsilon\Omega_0^2 = \frac{q_T^2 N}{\epsilon_0 \mu V} \quad , \tag{13}$$

$\frac{N}{V}$ being the density of oscillators, ϵ_0 the vacuum permittivity, and μ a reduced mass. In the general case, the plasma frequency can be experimentally determined from the real part of the optical conductivity (σ_1):

$$\Omega_p^2 = \frac{2}{\pi\epsilon_0}\int_{\omega_1}^{\omega_2}\sigma_1(\omega)d\omega \quad . \tag{14}$$

In equation 14 the equation limits are chosen to include only the area under the phonon response, and the free carrier or other electronic contributions must be subtracted from σ_1.

The Born charge (Z_k) is related to phonon plasma frequencies through:[14] [15]

$$\sum_k \frac{n_k Z_k^2}{m_k} = \epsilon_0 V \sum_j \Omega_{p,j}^2 \quad . \tag{15}$$

In Eq. 4, we made an approximation that all n_k atoms of the same species (mass m_k) have the same Born charge. V is the volume occupied by all atoms in the left hand side summation. The Born charge also respects charge neutrality:

$$\sum_k n_k Z_k = 0 \quad . \tag{16}$$

Equations 15 and 16 are enough to fully determine the Born charge in isotropic, binary compounds. In ternary materials, one must have an educated guess for the value of the Born charge of one of the atomic species. Fig. 4 in the main text shows the optical conductivity extracted from the variational dielectric function of the two films presented in Fig. 4. The shaded area shows the spectral weight that enters Eq. 14 in the determination of the phonon plasma frequency. From this area, we calculated the Born effective charge for the $(Sb_2Te_3)/(Sb_2Se_3)$ utilizing Eqs. 15 and 16. To account for the differences between Se and Te, we calculated the Born charge assuming that the film is either fully (Sb_2Te_3) or fully (Sb_2Se_3). We then took a weighted average of the two values. For the amorphous sample of $Sb_2Se_{.45}Te_{2.55}$, we obtained $Z_{Sb} = 3.76e$ and $Z_{Te/Se} = -2.51e$. In the crystalline, conducting sample of $Sb_2Se_{.45}Te_{2.55}$ we found $Z_{Sb} = 8.28e$ and $Z_{Te/Se} = -5.52e$.

Table I lists Z* and ε_∞ for amorphous and crystalline GeTe and GeSe. This table shows that both Z* and ε_∞ only show a modest increase upon crystallization for GeSe, while a much larger increase of both quantities is found for GeTe. Hence, GeTe is metavalent, while GeSe is covalent according to the three characteristic bond indicators aside of the PME discussed earlier:

i. high values of the Born effective charge Z*
ii. a large electronic polarizability, i.e. a high optical dielectric constant ε_∞ for the crystalline state
iii. a pronounced difference for Z* and ε_∞ between the amorphous and the crystalline state.

Table I: Z* and ϵ_∞ values for GeTe and GeSe in their amorphous (a-) and crystalline (c-) phases.

	Z^* / e	ϵ_∞
a-GeTe	2.0	13.2
c-GeTe	- (4.6)*	31.5 (38.8)*
a-GeSe	2.4	9.7
c-GeSe	3.6	13.5

* The values in brackets are results of DFT calculations[5] and have been averaged using a square average of the form $Z_{mean} = \sqrt{\frac{Z_{xx}^2+Z_{yy}^2+Z_{zz}^2}{3}}$.

References

[1] H.Bärnighausen, *Match9* **1980**, 9.
[2] J. A. Muir, R. J. Cashman, *Journal of Physics and Chemistry of Solids* **1967**, 28.
[3] H. Wiedemeier, P. A. Siemers, *High Temperature Science* **1984**, 17.
[4] M. Kupers, P. M. Konze, S. Maintz, S. Steinberg, A. M. Mio, O. Cojocaru-Miredin, M. Zhu, M. Muller, M. Luysberg, J. Mayer, M. Wuttig, R. Dronskowski, *Angewandte Chemie-International Edition* **2017**, 56.
[5] R. S. Halford, *Journal of Chemical Physics* **1946**, 14.
[6] W.H. Weber, R. Merlin, *Raman Scattering in Materials Science*, Springer **2000**.
[7] B. Huang, J. Robertson, *Physical Review B* **2010**, 81, 081204.
[8] M. Zhu, O. Cojocaru-Miredin, A. M. Mio, J. Keutgen, M. Kupers, Y. Yu, J. Y. Cho, R. Dronskowski, M. Wuttig, *Advanced Materials* **2018**, 30, 1706735.
[9] Y. D. Cheng, O. Cojocaru-Miredin, J. Keutgen, Y. Yu, M. Kupers, M. Schumacher, P. Golub, J. Y. Raty, R. Dronskowski, M. Wuttig, *Advanced Materials* **2019**, 31, 1904316.
[10] M. Gajdoš, K. Hummer, G. Kresse, J. Furthmüller, F. Bechstedt, *Physical Review B* **2006**, 73.
[11] S. Maier, S. Steinberg, Y. D. Cheng, C. F. Schon, M. Schumacher, R. Mazzarello, P. Golub, R. Nelson, O. Cojocaru-Miredin, J. Y. Raty, M. Wuttig, *Advanced Materials* **2020**, 32, 2005533.
[12] N. Ashcroft, D. Mermin, *Solid State Physics*, Cengage Learning, **1976**.
[13] M. Dressel, G. Grüner, *Electrodynamics in Solids*, Cambridge University Press, UK **2002**.
[14] J. F. Scott, *Physical Review B* **1971**, 4.
[15] X. Gonze, C. Lee, *Physical Review B* **1997**, 55.

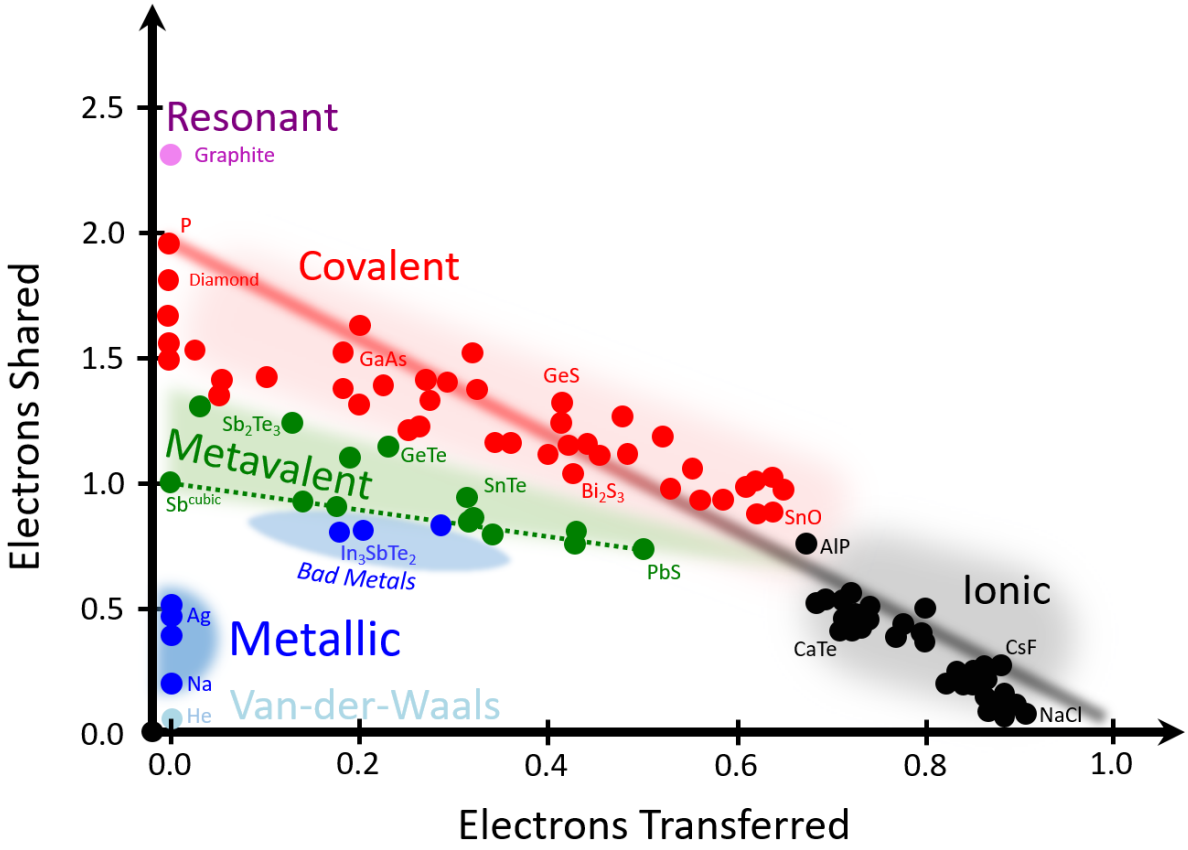
Resonant
Graphite
Covalent
P
Diamond
GaAs
GeS
Sb2Te3
Metavalent
GeTe
SnTe
Bi2S3
SnO
AlP
Sbcubic
In3SbTe2
Bad Metals
PbS
Ionic
Ag
Metallic
CaTe
CsF
Na
Van-der-Waals
He
NaCl
Electrons Shared
Electrons Transferred
0.0
0.5
1.0
1.5
2.0
2.5
0.0
0.2
0.4
0.6
0.8
1.0